



# NAVAL POSTGRADUATE SCHOOL

MONTEREY, CALIFORNIA

## THESIS

**LAGUERRE-GAUSSIAN MODES  
IN THE FREE ELECTRON LASER**

by

Anastasios Kampouridis

June 2007

Thesis Advisor:  
Co-Advisor:

William B. Colson  
Robert L. Armstead

**Approved for public release; distribution is unlimited**

THIS PAGE INTENTIONALLY LEFT BLANK

REPORT DOCUMENTATION PAGE			Form Approved OMB No. 0704-0188	
Public reporting burden for this collection of information is estimated to average 1 hour per response, including the time for reviewing instruction, searching existing data sources, gathering and maintaining the data needed, and completing and reviewing the collection of information. Send comments regarding this burden estimate or any other aspect of this collection of information, including suggestions for reducing this burden, to Washington headquarters Services, Directorate for Information Operations and Reports, 1215 Jefferson Davis Highway, Suite 1204, Arlington, VA 22202-4302, and to the Office of Management and Budget, Paperwork Reduction Project (0704-0188) Washington DC 20503.				
1. AGENCY USE ONLY (Leave blank)		2. REPORT DATE June 2007	3. REPORT TYPE AND DATES COVERED Master's Thesis	
4. TITLE AND SUBTITLE Laguerre-Gaussian Modes in the Free Electron Laser			5. FUNDING NUMBERS	
6. AUTHOR(S) Anastasios Kampouridis				
7. PERFORMING ORGANIZATION NAME(S) AND ADDRESS(ES) Naval Postgraduate School Monterey, CA 93943-5000			8. PERFORMING ORGANIZATION REPORT NUMBER	
9. SPONSORING /MONITORING AGENCY NAME(S) AND ADDRESS(ES) N/A			10. SPONSORING/MONITORING AGENCY REPORT NUMBER	
11. SUPPLEMENTARY NOTES The views expressed in this thesis are those of the author and do not reflect the official policy or position of the Department of Defense or the U.S. Government.				
12a. DISTRIBUTION / AVAILABILITY STATEMENT Approved for public release; distribution is unlimited			12b. DISTRIBUTION CODE	
13. ABSTRACT (maximum 200 words) In a free electron laser (FEL) system, knowing the optical beam characteristics is of great importance. A beam may be comprised of higher-order modes due to the interaction with the electron beam, or from non-ideal operational conditions such as mirror distortions and misalignments, or from imperfect injection of the electron beam. In this thesis, the basic FEL theory is initially reviewed. The parabolic wave equation is then solved for the "fundamental" Gaussian mode and for higher-order modes. Working in rectangular coordinates, a complete and orthogonal set of solutions involving Hermite polynomials is found. When the wave equation is solved in cylindrical coordinates, we arrive at a set of solutions that contain Laguerre polynomials. The so-called Laguerre-Gaussian modes are analyzed. The evolution of these laser modes is also explored, yielding quite unexpected results due to their phase structure and orbital angular momentum of light. Lastly, we study a common case where higher-order optical modes appear, in order to quantify the tolerances of an FEL.				
14. SUBJECT TERMS Free Electron Laser, High Order Modes, Laguerre-Gaussian Optical Modes.			15. NUMBER OF PAGES 87	
			16. PRICE CODE	
17. SECURITY CLASSIFICATION OF REPORT Unclassified	18. SECURITY CLASSIFICATION OF THIS PAGE Unclassified	19. SECURITY CLASSIFICATION OF ABSTRACT Unclassified	20. LIMITATION OF ABSTRACT UL	

THIS PAGE INTENTIONALLY LEFT BLANK

**Approved for public release; distribution is unlimited**

**LAGUERRE-GAUSSIAN MODES  
IN THE FREE ELECTRON LASER**

Anastasios Kampouridis  
Major, Hellenic Air Force  
B.S., Hellenic Air Force Academy, 1991

Submitted in partial fulfillment of the  
requirements for the degree of

**MASTER OF SCIENCE IN PHYSICS**

from the

**NAVAL POSTGRADUATE SCHOOL  
June 2007**

Author: Anastasios Kampouridis

Approved by: William B. Colson  
Thesis Advisor

Robert L. Armstead  
Co-Advisor

James H. Luscombe  
Chairman, Department of Physics

THIS PAGE INTENTIONALLY LEFT BLANK

## ABSTRACT

In a free electron laser (FEL) system, knowing the optical beam characteristics is of great importance. A beam may be comprised of higher-order modes due to the interaction with the electron beam, or from non-ideal operational conditions such as mirror distortions and misalignments, or from imperfect injection of the electron beam.

In this thesis, the basic FEL theory is initially reviewed. The parabolic wave equation is then solved for the “fundamental” Gaussian mode and for higher-order modes. Working in rectangular coordinates, a complete and orthogonal set of solutions involving Hermite polynomials is found. When the wave equation is solved in cylindrical coordinates, we arrive at a set of solutions that contain Laguerre polynomials. The so-called Laguerre-Gaussian modes are analyzed. The evolution of these laser modes is also explored, yielding quite unexpected results due to their phase structure and orbital angular momentum of light. Lastly, we study a common case where higher-order optical modes appear, in order to quantify the tolerances of an FEL.

THIS PAGE INTENTIONALLY LEFT BLANK

# TABLE OF CONTENTS

I.	INTRODUCTION.....	1
II.	FREE ELECTRON LASER SYSTEM .....	3
A.	FEL CONFIGURATIONS .....	3
B.	FEL COMPONENTS .....	4
1.	Electron Beam Injector.....	5
2.	Accelerator .....	5
3.	Undulator .....	7
4.	Resonator .....	7
5.	Beam Dump.....	7
III.	BASIC FREE ELECTRON LASER THEORY .....	9
A.	FEL PENDULUM EQUATION .....	9
B.	DIFFRACTION OF LASER BEAMS .....	18
C.	THE FEL WAVE EQUATION.....	22
D.	GAIN .....	25
IV.	OPTICAL THEORY .....	29
A.	FUNDAMENTAL SOLUTION TO THE WAVE EQUATION.....	29
B.	PROPERTIES AND PROPAGATION OF GAUSSIAN BEAMS .....	35
V.	HIGHER ORDER MODES .....	39
A.	HERMITE-GAUSSIAN MODES .....	39
B.	LAGUERRE-GAUSSIAN MODES .....	42
C.	LAGUERRE-GAUSSIAN MODE ANALYSIS .....	48
1.	Intensity Plots .....	48
2.	Plots of Real Part.....	50
D.	PROPAGATION OF LAGUERRE-GAUSSIAN MODES.....	52
1.	Intensity Plots .....	52
2.	Plots of Real Part .....	54
VI.	HIGH-ORDER MODES IN FREE ELECTRON LASER SIMULATIONS.....	59
A.	ELECTRON BEAM TILT.....	59
1.	Gain.....	60
2.	Extraction .....	64
VII.	CONCLUSION .....	69
	LIST OF REFERENCES.....	71
	INITIAL DISTRIBUTION LIST .....	73

THIS PAGE INTENTIONALLY LEFT BLANK

## LIST OF FIGURES

Figure 1.	Schematic of Jefferson Lab free electron laser After [1].	2
Figure 2.	Oscillator Free Electron Laser From [2].	3
Figure 3.	SASE Free Electron Laser From [2].	4
Figure 4.	Electron Injector After [3].	5
Figure 5.	JLab Superconducting LINAC (a), (b) A five-cell cavity, photo and sketch, (c) Part of a cryomodule which contains six five-cell cavities From [4].	6
Figure 6.	Schematic diagram of the electron beam dump After [5].	8
Figure 7.	Phase Space evolution of Electrons at Resonance ( $\nu_o = 0$ ), corresponding optical field Gain and Phase evolution.	17
Figure 8.	Phase Space evolution of Electrons injected off resonance ( $\nu_o = 2.6$ ), corresponding optical field Gain and Phase evolution.	17
Figure 9.	Single pass gain versus initial electron phase velocity $\nu_o$ at $\tau = 1$ .	28
Figure 10.	Cross-section of a propagating Gaussian Beam.	33
Figure 11.	Gaussian beam profile.	34
Figure 12.	Cross-section of a propagating Gaussian Beam with $\tau_w = 0$ and $z_o = 0.3$ .	36
Figure 13.	Surface plots of a Gaussian Beam evolution at times (a) $\tau = 0$ , (b) $\tau = 0.5$ and (c) $\tau = 1$ . Scales in z-axis are different.	37
Figure 14.	Hermite-Gaussian modes in the transverse plane $x, y$ . Red indicates highest intensity, while blue indicates least intensity.	41
Figure 15.	Laguerre-Gaussian modes $LG_p^l$ ; Intensity plots ( $a_{p,l} \times a_{p,l}^*$ ) in the transverse plane $x, y$ , at $\tau = 0$ , where red is most intense, while blue is least intense.	49
Figure 16.	Radial intensity distribution for (a) $LG_2^1$ and (b) $LG_3^2$ beams.	50
Figure 17.	Laguerre-Gaussian modes $LG_p^l$ ; plots of the real part squared, at $\tau = 0$ .	51
Figure 18.	Intensity plots of Laguerre-Gaussian modes as they propagate.	53
Figure 19.	Plots of (a) real part and (b) real part squared of a $LG_0^3$ beam at the end of the propagation distance ( $\tau = 1$ ), with $a_o = 1$ and $z_o = 0.4$ .	55
Figure 20.	Plots of (a) real part and (b) real part squared of a $LG_1^2$ beam at the end of the propagation distance ( $\tau = 1$ ), with $a_o = 1$ and $z_o = 0.4$ .	55
Figure 21.	Plots of (a) real part and (b) real part squared of a $LG_2^1$ beam at the end of the propagation distance ( $\tau = 1$ ), with $a_o = 1$ and $z_o = 0.4$ .	56
Figure 22.	Radial distribution of a $LG_2^1$ beam along (a) $\vartheta = 0$ , (b) $\vartheta = \pi/2$ and (c) $\vartheta = \pi/4$ .	57
Figure 23.	Set of points in $r$ and $\vartheta$ where the cosine term of equation (V.33) is maximum.	57

Figure 24.	Simulation output, showing the power $P$ versus number of passes $n$ in an FEL. In the first region, power is still building up while in region 2, FEL has reached its steady-state. ....	60
Figure 25.	Output of a 3-D Simulation for Jefferson Lab FEL. ....	63
Figure 26.	Summary of the simulation results for the gain versus increasing electron beam tilt angle $\tilde{\theta}_{y_0}$ . ....	64
Figure 27.	Output of a 3-D Simulation for Jefferson Lab FEL, exploring extraction. ....	66
Figure 28.	Summary of the simulation results for the extraction $\eta$ versus increasing electron beam tilt angle $\tilde{\theta}_{y_0}$ . ....	67

## LIST OF TABLES

Table 1.	Hermite polynomials .....	41
Table 2.	Associated Laguerre polynomials From [9]. .....	46
Table 3.	The basic dimensionless parameters used in the Jefferson Lab FEL simulations for the Gain.....	61
Table 4.	The basic dimensionless parameters used in the Jefferson Lab FEL simulations for the extraction.....	65

THIS PAGE INTENTIONALLY LEFT BLANK

# I. INTRODUCTION

The Free Electron Laser (FEL) is a source of powerful, coherent radiation with unique attributes. Continuous tunability, high power, good efficiency and reliability make it suitable for a wide span of applications. The option of high power derives in part from the absence of a medium vulnerable to damage.

Powerful coherent radiation was first produced when the microwave tube, which uses a beam of free non-relativistic electrons inside a closed microwave cavity, was invented in the 1930's. Following this invention, the introduction of the open resonator enabled many steps towards the development of more powerful and efficient radiation sources.

Based on its special attributes, the FEL is suitable for many diverse applications. It can be used in biology to study cell and molecular structure, and it can be used in the military, due to its high power output and its capability to operate in a broad range of wavelengths. A critical requirement for an FEL to have the desired results is good optical beam quality. We need to know the beam shape that can be produced under various operational conditions, so as to evaluate its performance.

In this thesis, we analyze various high-order modes from an FEL, emphasizing cylindrical coordinates, which are motivated by the symmetry of the system. We present a brief review of a typical FEL system in the first chapter, as well as the relevant operating configurations. The next chapter introduces basic FEL theory, where we derive the pendulum equation, which describes the electron motion, and the parabolic wave equation, which describes the laser light evolution, from the classical electromagnetic theory.

In the chapters that follow, we focus our attention on the optical beam. First, the basic optical theory is reviewed and the fundamental-mode solution to the wave equation is derived and analyzed. Although this solution is a good approximation for the output of many FELs, the actual operating parameters of a

system can generate laser light with higher-order modes. To analyze this effect, we initially review work with rectangular coordinates, and find the Hermite-Gaussian modes. Following this, new work is presented with cylindrical coordinates, which are more relevant to an FEL system, and we arrive at the Laguerre-Gaussian solutions. Analyzing these high-order modes, we find that the orbital angular momentum of light plays important role in the evolution of such a beam.

In the last chapter, we present the results of a new set of simulations designed to investigate the tolerance of the Jefferson Lab FEL (Figure 1) to electron beam tilt. From these results, we see that higher-order optical modes do indeed appear as a consequence of the non-ideal operating conditions.

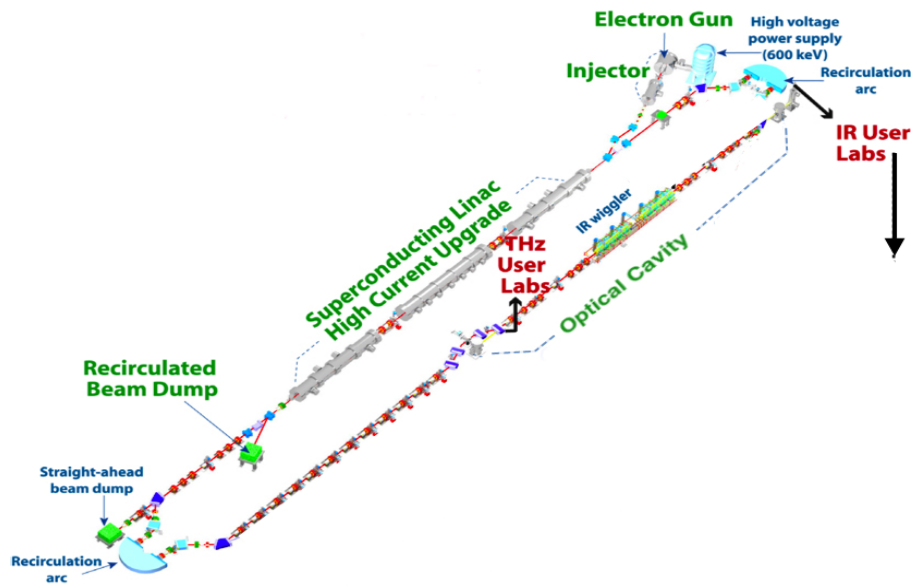


Figure 1. Schematic of Jefferson Lab free electron laser After [1].

## II. FREE ELECTRON LASER SYSTEM

In the Free Electron Laser, a beam of relativistic electrons, produced by an injector and accelerated by a linear electron accelerator, passes through a transverse, periodic magnetic field, called the undulator, oscillates and therefore radiates. Radiation can be captured in a cavity and used to induce new electrons to emit even more radiation. Alternatively, radiation from an external source can be amplified over a single pass, and even without an external source it is possible to produce radiation through the process of spontaneous emission. Therefore, it is informative to look at the possible basic setups, which can be used in order for a free electron laser system to function.

### A. FEL CONFIGURATIONS

The configuration used in the first FEL by John Madey in 1977 is the *oscillator*, employing an optical cavity in a very similar way as in the conventional chemical or solid state lasers. Radiation is stored and amplified in the optical cavity, bracketed by one fully and one partially reflective mirror, the latter being used to outcouple the laser light. Coherence is established after many passes of the light. Figure 2 is a typical FEL oscillator, where the emphasis is placed on the resonator.

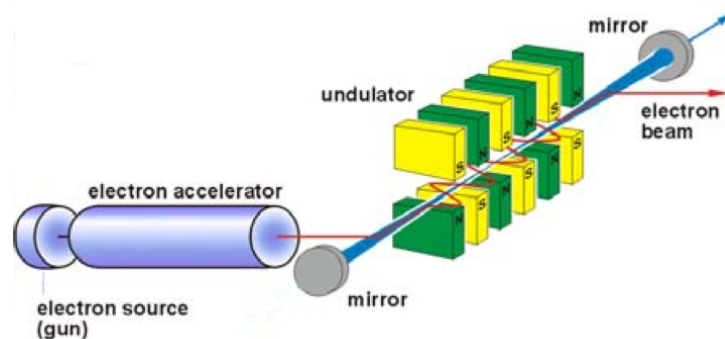


Figure 2. Oscillator Free Electron Laser From [2].

In the *amplifier* configuration there is no optical resonator and it can be considered the simplest type of FEL. Light from a seed laser is amplified by the interaction with the electron beam, passing only once through the periodic magnetic field. Coherence in this case is set up by the seed laser.

A special type of amplifier is the SASE FEL (Self-Amplified Spontaneous Emission) where there is no external source. Instead, the spontaneous radiation in the first part of the magnetic field is used as the seed laser. At present, it appears to be the most promising concept in the race towards achieving much shorter wavelengths (UV,X-rays), since there are no seed lasers in this regime. Figure 3 shows the layout of a SASE FEL, where there are neither resonator mirrors nor seed laser, but where a significantly longer undulator is required.

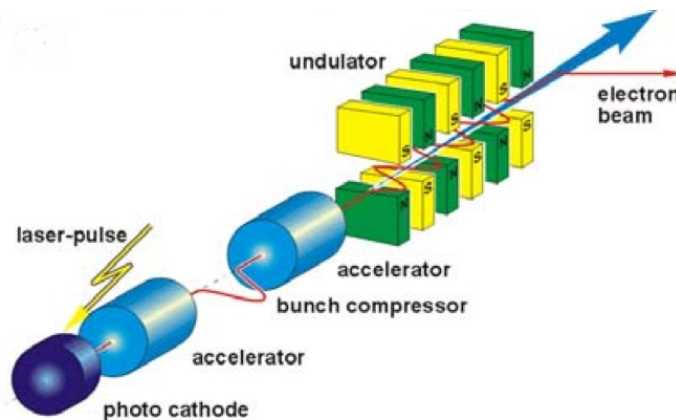


Figure 3. SASE Free Electron Laser From [2].

## B. FEL COMPONENTS

The major components of an FEL system are the electron beam source, the accelerator, the undulator, the resonator (for the oscillator) and the beam dump. There are many other elements that make an FEL system operational, like bending and control magnets to steer the electron beam in the desired path and several detecting devices to continuously monitor all the critical points, in order to

keep track of the operational parameters and to enhance the performance. Last but not least, an optical system must be utilized to transport the laser light in the desired area.

## 1. Electron Beam Injector

The electron beam injector is the original source of electrons in the FEL, and it plays a crucial roll in the performance of the system. It is usually a photoinjector, where a drive laser excites the electrons in a cathode, which is positioned inside a Radio Frequency (RF) cavity, and a high voltage is applied so as to accelerate the released electrons, allowing them to gain a modest amount of energy before entering the main accelerator. Instead of taking advantage of the photoelectric effect, much the same release of electrons can be obtained by heating the cathode. The electron beam that is produced from an injector, like the one shown in Figure 4, usually comes out in pulses at regular intervals.

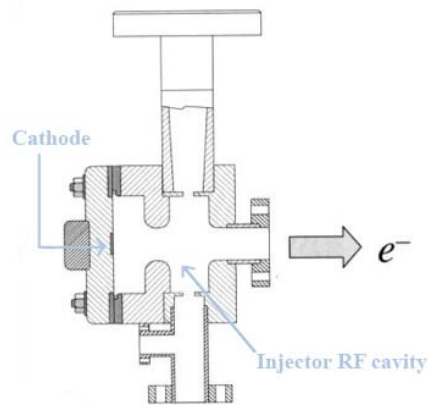


Figure 4. Electron Injector After [3].

## 2. Accelerator

The electrons emerge from the injector with energy of about 5-10 MeV. In order to achieve infrared radiation from the FEL, we need a relativistic electron beam of about 100 MeV. To attain this energy level, the electron beam is passed through a Radio Frequency Linear Accelerator (RF LINAC). Superconducting

technology may be used as in the JLab FEL LINAC, shown in Figure 5. The accelerator uses an alternating electric field, which interacts with each electron bunch that passes through the RF cavity. For this reason, the electric field has to be fully synchronized with the electron bunches, so that it continuously accelerates the electrons. Also, the accelerator must have several stages of RF modules in order for the electrons to reach the required energy.

The RF field inside the linear accelerator is generated by a klystron. To reduce the input power required, a special technique has been introduced. The electron beam that has traveled through the whole system can be driven back through the accelerator, so as to give most of its remaining energy, back to the RF field. To achieve this, we have to carefully adjust the timing of the beam, so as to be out of phase with the electric field of the RF cavities. This energy recovery procedure through the recirculation of the electron beam increases the overall efficiency of the system and additionally reduces the beam dump size.

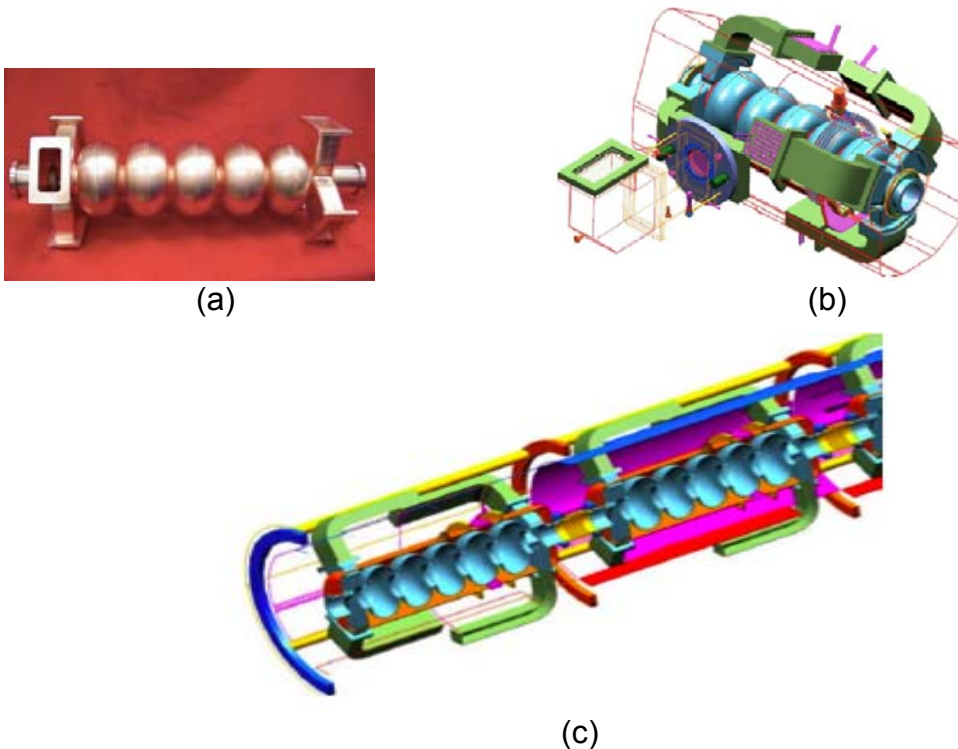


Figure 5. JLab Superconducting LINAC (a), (b) A five-cell cavity, photo and sketch, (c) Part of a cryomodule which contains six five-cell cavities From [4].

### **3. Undulator**

The undulator is the component of the FEL system that forces the electron beam to wiggle and radiate. It is composed of a group of magnets, as can be seen in Figures 2 and 3, arranged so that they form an alternating magnetic field along the axis of the undulator. The electrons leaving the accelerator with relativistic speeds, enter the periodic magnetic field of the undulator, where the Lorentz force drives them to oscillate in a transverse direction. The radiation that is emitted interacts with the light already present in the undulator, through the process of the stimulated emission. This interaction results in the amplification of the stored light.

### **4. Resonator**

In the oscillator configuration, as the one shown in Figure 2, the FEL system makes use of an optical cavity with the undulator enclosed inside. This way, light is stored and amplified through many passes. Two mirrors bound the cavity: one of them totally reflects the light, while the other allows a percentage to come out. The light that emerges through this out-coupling mirror is the desired, usable laser light of the system. It is obvious that for maximum coupling efficiency between the electrons and the light within the resonator, the optical beam should be synchronized with the electron bunch.

### **5. Beam Dump**

The beam dump is simply a notched piece of metal that absorbs the energy of the electrons at the end of their path, either just after the undulator or in the energy recovery configuration, after the linear accelerator. Even though electrons give energy to the optical field in order for the FEL to emit light, and probably back to the RF field, they still have energy to be removed. Therefore, the beam dump can heat up at megawatt rates and needs to be water-cooled. Furthermore, it is shielded so that no radiation can exit. A schematic diagram of a beam dump is shown in Figure 6.

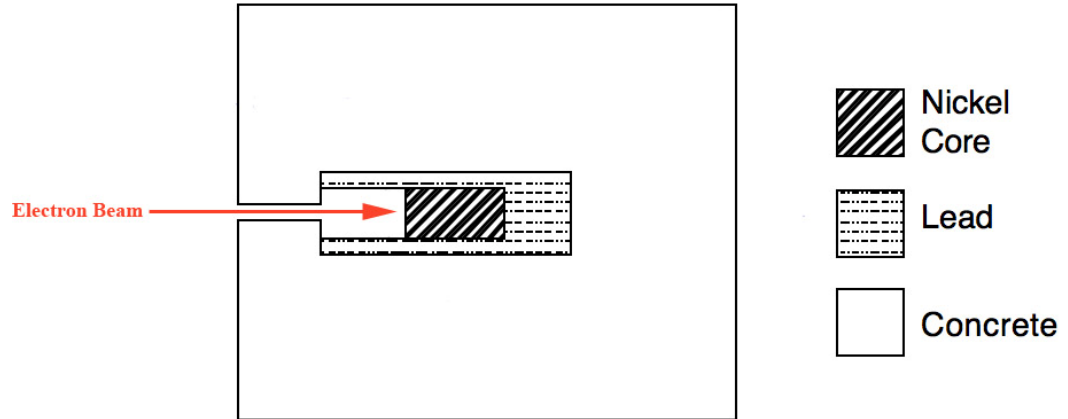


Figure 6. Schematic diagram of the electron beam dump After [5].

### III. BASIC FREE ELECTRON LASER THEORY

The basic idea behind the operation of a free electron laser is the extraction of energy from relativistic electrons, forcing them to radiate coherently. This energy conversion takes place inside the undulator, where the electron beam makes a wiggling, transverse motion, emitting spontaneous radiation in the forward direction. We can couple this motion to the electric field of the radiation to produce stimulated emission, thus amplifying the optical mode. We will now look at the mathematics that describe the attributes of a free electron laser and explain its operation.

#### A. FEL PENDULUM EQUATION

In order to understand the physics behind the electron motion and the subsequent radiation, we will first study their behavior inside the magnetic field of the undulator. For that reason, we will consider relativistic electrons entering a helical undulator field along the z-axis in the presence of optical field. As the electrons travel along the undulator, forces from both the static magnetic field of the undulator, and the oscillating electric and magnetic fields of the optical mode affect them [6].

The magnetic field of the undulator can be expressed in rectangular coordinates as:

$$\vec{B}_U = B(\cos(k_o z), \sin(k_o z), 0), \quad (\text{III.1})$$

where  $B$  is the magnetic field strength,  $k_o = 2\pi/\lambda_o$  is the undulator wavenumber and  $\lambda_o$  is the undulator wavelength, being the distance of one complete cycle of the magnetic field in the undulator.

The corresponding electric and magnetic field of the optical wave are given by:

$$\vec{E} = E(\cos \psi, -\sin \psi, 0), \quad (III.2)$$

$$\vec{B} = E(\sin \psi, \cos \psi, 0), \quad (III.3)$$

with  $\psi = kz - \omega t + \varphi$ ,  $E$  the field amplitude of the optical wave in cgs units,  $k = \omega / c$  the optical wavenumber,  $\omega$  the frequency and  $\varphi$  the optical phase.

Electrons entering these fields encounter a Lorentz force that, in the case of relativistic particles, is given by the equations

$$\frac{d(\gamma \vec{\beta})}{dt} = -\frac{e}{mc} (\vec{E} + \vec{\beta} \times \vec{B}), \quad (III.4)$$

$$\frac{d\gamma}{dt} = -\frac{e}{mc} \vec{\beta} \cdot \vec{E}, \quad (III.5)$$

where  $\gamma = 1/\sqrt{1-\vec{\beta}^2}$  is the Lorentz factor,  $\vec{\beta} = \vec{v}/c$  is the dimensionless electron velocity,  $e = |e|$  is the electron charge magnitude and  $m$  is the electron rest mass. Equation (III.5) is also known as the energy equation because it describes how electrons exchange energy with the optical field, and the electron energy is  $\varepsilon = \gamma mc^2$ .

We can now substitute the fields from (III.1)-(III.3) into (III.4) to obtain the spatial components of the force on the electron

$$\frac{d(\gamma \vec{\beta}_\perp)}{dt} = -\frac{e}{mc} [E(1-\beta_z)(\cos \psi, -\sin \psi, 0) + \beta_z B(-\sin k_o z, \cos k_o z, 0)], \quad (III.6)$$

$$\frac{d(\gamma \beta_z)}{dt} = -\frac{e}{mc} [E(\beta_x \cos \psi - \beta_y \sin \psi) + B(\beta_x \sin k_o z - \beta_y \cos k_o z)], \quad (III.7)$$

where  $\beta_x, \beta_y, \beta_z$  are the three components of the velocity and  $\vec{\beta}_\perp = \beta_x \hat{i} + \beta_y \hat{j}$  is the transverse velocity. Since we are dealing with relativistic electrons, we can take  $\beta_z \approx 1$ . Then, all terms of  $E(1 - \beta_z)$  are small compared to  $\beta_z B$  and can be dropped. Integrating (III.6) and assuming perfect injection into helical orbits, so as to take the constants of integration to be zero, we obtain the velocity of the transverse motion

$$\vec{\beta}_\perp = -\frac{eB\lambda_o}{2\pi\gamma mc^2} (\cos k_o z, \sin k_o z, 0). \quad (\text{III.8})$$

We can write (III.8) in a more compact form if we introduce the dimensionless undulator parameter

$$K = \frac{eB_{rms}\lambda_o}{2\pi mc^2}, \quad (\text{III.9})$$

with  $B_{rms}$  the rms value of the undulator magnetic field. Then

$$\vec{\beta}_\perp = -\frac{K}{\gamma} (\cos k_o z, \sin k_o z, 0). \quad (\text{III.10})$$

In (III.10) note that for the helical undulator,  $B_{rms} = B$  and for a linearly polarized undulator  $B_{rms} = B/\sqrt{2}$ .

At this point, we are able to look at the basic transverse motion of the electrons, by making the assumption that they travel roughly with the speed of light along the undulator. Then  $\beta_z c \approx c$ , and taking the electron velocity to be constant we can write  $z(t) \approx \beta_z ct$ . Using  $\omega_o = \beta_z k_o c \approx k_o c$  as the electron oscillation frequency, (III.10) becomes

$$\vec{\beta}_\perp \approx -\frac{K}{\gamma} (\cos(\omega_o t), \sin(\omega_o t), 0), \quad (\text{III.11})$$

and integrating we get

$$\vec{x}_{\perp}(t) \approx \frac{K}{\gamma} \frac{\lambda_o}{2\pi} (-\sin(\omega_o t), \cos(\omega_o t), 0), \quad (\text{III.12})$$

with  $\vec{x}_{\perp}(t) = x(t)\hat{i} + y(t)\hat{j}$ . This equation approximates the transverse motion of the electrons inside the undulator. From this expression and for typical systems, we find that electrons move in the transverse directions in a distance of about  $25 \mu\text{m}$ , the oscillation frequency is in the microwave regime, but due to the relativistic *Doppler effect*, the radiation frequency is multiplied by a factor of  $\gamma^2$ , resulting in lasing at much higher infrared frequencies.

Next, we want to study more carefully the microscopic motion of the electrons, without making the approximations of the previous paragraph. For this reason, we will use the transverse motion we found in equation (III.10), and plug it into the energy equation (III.5) to get

$$\dot{\gamma} = \frac{d\gamma}{dt} = -\frac{e}{mc} E (\beta_x \cos \psi - \beta_y \sin \psi). \quad (\text{III.13})$$

Introducing the electron phase  $\zeta = (k + k_o)z - \omega t$  and recalling that  $\psi = kz - \omega t + \varphi$ , (III.13) is rewritten as

$$\dot{\gamma} = \frac{eKE}{\gamma mc} \cos(\zeta + \varphi). \quad (\text{III.14})$$

The last equation describes energy exchange, because it tells us whether electrons lose or gain energy, based on the sign of the  $\cos(\zeta + \varphi)$  term. For instance, when  $\cos(\zeta + \varphi) < 0$  then  $\dot{\gamma} < 0$ , thus electron energy  $\varepsilon = \gamma mc^2$  decreases, which is the desired condition for the FEL to operate, so that electrons give energy to the optical field.

Electron phase  $\zeta$  is a way to relate electron position to the co-propagating optical field; it corresponds to the position of the electron in a section of the electron beam one optical wavelength long. Therefore, it is reasonable to introduce the electron phase velocity, defined in the following way so as to be dimensionless

$$\nu \equiv \dot{\zeta} \frac{L}{c} = L[(k+k_o)\beta_z - k] = \dot{\zeta}, \quad (\text{III.15})$$

where  $L = N\lambda_o$  is the length of the undulator,  $N$  is the number of undulator periods and the symbol  $\dot{(\cdot)}$  indicates the derivative with respect to the dimensionless time  $\tau$ , defined by  $\tau = ct/L$ . This normalizes time to the length of the undulator, so that  $\tau = 0 \rightarrow 1$  from the beginning to the end of the undulator.

The dimensionless electron phase velocity  $\nu$  is also known as the “resonance parameter”. For an electron that satisfies the resonance condition  $\nu = 0$ , the electrons and optical field have optimum energy exchange. In this case,  $c\beta_z = kc/(k+k_o)$ . Assuming again relativistic electrons, we have  $\beta_z \approx 1$  and  $k \gg k_o$ . Therefore,  $\lambda = \lambda_o$  and laser frequency  $\omega \gg \omega_o$ , where  $\omega_o \approx 2\pi c/\lambda_o$  is the electron oscillation frequency. Then, the laser wavelength is

$$\lambda = \frac{\lambda_o(1-\beta_z)}{\beta_z}. \quad (\text{III.16})$$

From (III.10), we find that  $\beta_{\perp}^2 = K^2/\gamma^2$  and so

$$\beta_z = \left(1 - \frac{1+K^2}{\gamma^2}\right)^{1/2}. \quad (\text{III.17})$$

For relativistic electrons with  $\gamma \gg 1$ , equation (III.17) can be approximated by

$$\beta_z \approx 1 - \frac{1 + K^2}{2\gamma^2}. \quad (\text{III.18})$$

Combining equations (III.16) and (III.18) we find the following expression of the resonance condition for the laser wavelength

$$\lambda = \frac{\lambda_o (1 + K^2)}{2\gamma^2}. \quad (\text{III.19})$$

This resonance relationship makes obvious that an FEL can be continuously tuned by changing physical parameters, like the electron energy  $\varepsilon = \gamma mc^2$  or the design of the undulator. Since the undulator parameter is typically  $K \approx 1$ , it is clear that optical wavelength is much smaller than that of the undulator by a factor of approximately  $1/\gamma^2$ .

We are able now to continue our analysis, so as to arrive to a compact expression for the electron microscopic motion, taking first the time derivatives of the electron phase velocity  $v$ , defined in (III.15) and that of the longitudinal velocity  $\beta_z$  from (III.18)

$$\dot{v} = L(k + k_o) \dot{\beta}_z, \quad \dot{\beta}_z = \frac{1 + K^2}{\gamma^3} \dot{\gamma}. \quad (\text{III.20})$$

Then, we combine these results to find  $\dot{v} = 4\pi N \dot{\gamma} / \gamma$  and finally substituting  $\dot{\gamma}$  from (III.14) we get

$$\dot{v} = \frac{L}{c} \dot{v} = \zeta = \frac{4\pi NeKLE}{\gamma^2 mc^2} \cos(\zeta + \varphi). \quad (\text{III.21})$$

It is now reasonable to collect terms and define  $|a| = 4\pi NeKLE / \gamma^2 mc^2$  as the dimensionless laser field amplitude, so that (III.21) becomes

$$\dot{\nu} = \dot{\zeta} = |a| \cos(\zeta + \varphi), \quad (\text{III.22})$$

which is the FEL “pendulum equation” that describes the microscopic motion of each electron in the reference frame of one optical wavelength. In this reference frame, the motion of the electrons can be taken to be similar to a classical pendulum. The dimensionless laser field amplitude  $|a|$  is a measure of the strength of the optical field and expresses the rate of the electron bunching. When  $|a| \gg \pi$  the laser has strong fields and it is near saturation, while for  $|a| \leq \pi$  the optical field is weak and there is no overbunching of electrons.

Equation (III.22) implies that electrons inside the magnetic field of the undulator move in an equivalent way to the classical pendulum. Phase space plots are commonly utilized to visualize the motion of a pendulum, thus they can also be used to describe the motion of the electrons within an optical wavelength, showing the evolution of electron phase and phase velocity (analogous to position and angular velocity for the classical pendulum). Since phase velocity is related to the energy, phase space plots give an informative picture of the energy exchange between electrons and the optical field.

The following figures show the phase space paths for 20 sample electrons, injected with the same initial phase velocity, and having uniformly distributed initial phase. The FEL phase space paths can be found from the expression [6]

$$\nu^2 = \nu_o^2 + 2|a|[\sin(\zeta + \varphi) - \sin(\zeta_o + \varphi)], \quad (\text{III.23})$$

while the separatrix is given by

$$\nu^2 = 2|a|[1 + \sin(\zeta + \varphi)] \quad \text{i.e.,} \quad \nu = \pm \sqrt{2|a|}[1 + \sin(\zeta + \varphi)]^{1/2}, \quad (\text{III.24})$$

which defines a closed contour inside of which are the closed orbits, and outside of which are the open orbits. It passes through the unstable fixed points  $(\zeta, \nu) = (-\pi/2, 0)$  and  $(\zeta, \nu) = (3\pi/2, 0)$ , and its peak to peak height is easily seen to be  $4|a|^{1/2}$ . An electron moving in an open orbit corresponds to a pendulum that swings over the top, whereas an electron that follows a closed orbit corresponds to a pendulum that swings back and forth.

In Figure 7 it is plotted the evolution of 20 sample electrons starting at resonance ( $\nu_o = 0$ ), during the time period from  $\tau = 0$  (appearing as yellow dots) to  $\tau = 1$  (appearing as red dots). All paths are inside the separatrix, thus all electrons follow closed paths. The symmetry that appears, indicates that half of the electrons gain energy from the optical field and their paths shift up, while the other half lose energy. This is represented in the same figure from the graph of the net gain  $G(\tau)$ , which is almost zero. Gain is defined as

$$G(\tau) = \frac{P(\tau) - P_o}{P_o}, \quad (\text{III.25})$$

where  $P(\tau)$  is the optical power at time  $\tau$  and  $P_o$  is the initial power. The optical phase evolution  $\varphi(\tau)$  is plotted in the same figure.

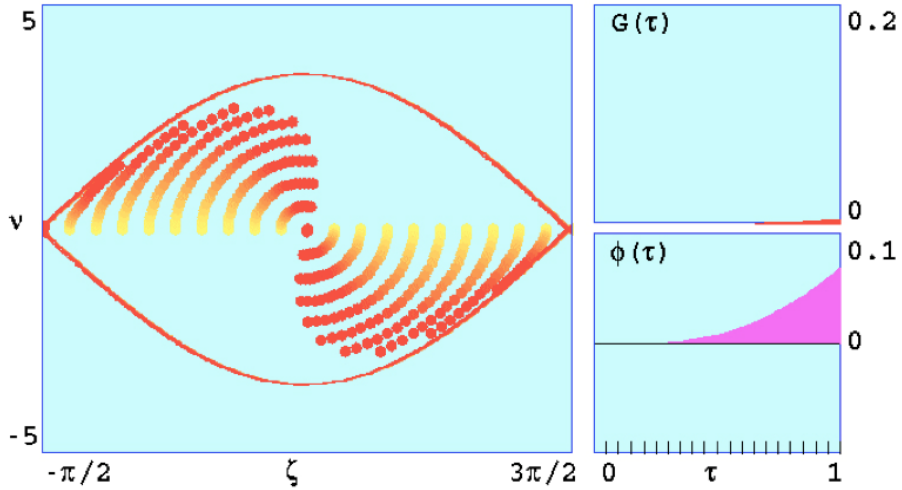


Figure 7. Phase Space evolution of Electrons at Resonance ( $v_o = 0$ ), corresponding optical field Gain and Phase evolution.

Contrary to the nearly zero net energy transfer when electrons are injected at resonance, we can arrange to have electrons give net energy to the optical field. Injecting electrons slightly off resonance, as shown in Figure 8, we notice that while some of them perform open orbits, at the end of the undulator when  $\tau = 1$ , most electrons have moved to a lower value of phase velocity, resulting in a net loss of energy. In this case, a very important effect takes place near  $\zeta = \pi$ , namely “bunching” of the electrons and a final gain of more than 10%.

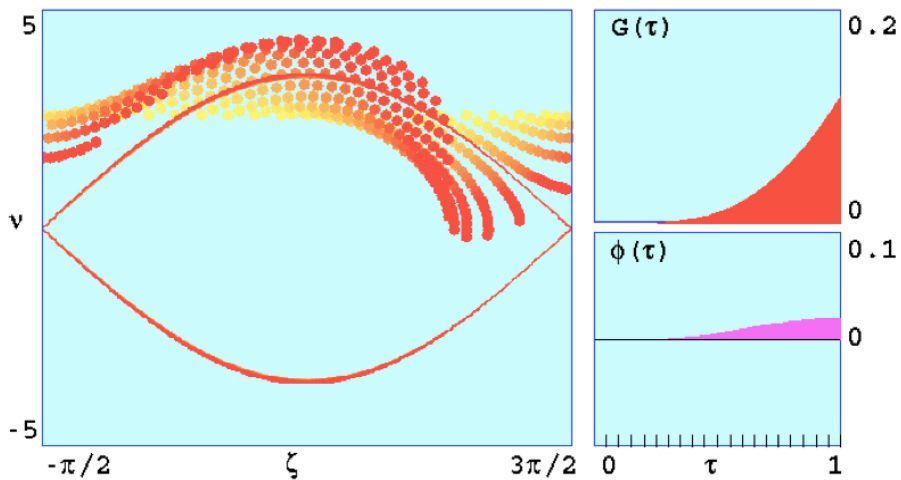


Figure 8. Phase Space evolution of Electrons injected off resonance ( $v_o = 2.6$ ), corresponding optical field Gain and Phase evolution.

## B. DIFFRACTION OF LASER BEAMS

We will now study the propagation of laser light through a sourceless medium, in order to be able to understand and describe how light travels and moreover, how is affected by diffraction. We start with Maxwell's equations, assuming for our case an isotropic and homogeneous medium. When there are no sources, that is to say the charge density  $\rho = 0$  and the current density  $j = 0$ , we write the four Maxwell's equations in cgs units as

$$\nabla \cdot \vec{E} = 0, \quad (III.26)$$

$$\nabla \cdot \vec{B} = 0, \quad (III.27)$$

$$\nabla \times \vec{E} = -\frac{1}{c} \frac{\partial \vec{B}}{\partial t}, \quad (III.28)$$

$$\nabla \times \vec{B} = \frac{1}{c} \frac{\partial \vec{E}}{\partial t}, \quad (III.29)$$

where  $c$  is the speed of light. Taking the curl of both sides of equation (III.28) we have

$$\begin{aligned} \nabla \times (\nabla \times \vec{E}) &= \nabla \times \left( -\frac{1}{c} \frac{\partial \vec{B}}{\partial t} \right) \\ &= -\frac{1}{c} \frac{\partial}{\partial t} (\nabla \times \vec{B}). \end{aligned}$$

Applying a vector identity on the left-hand side and substituting  $\nabla \times \vec{B}$  from (III.29), we get

$$\nabla (\nabla \cdot \vec{E}) - \nabla^2 \vec{E} = -\frac{1}{c} \frac{\partial}{\partial t} \left( \frac{1}{c} \frac{\partial \vec{E}}{\partial t} \right). \quad (III.30)$$

Then, since  $\nabla \cdot \vec{E} = 0$  from (III.26), we get

$$\left( \nabla^2 - \frac{1}{c^2} \frac{\partial^2}{\partial t^2} \right) \bar{E} = 0, \quad (\text{III.31})$$

which is the wave equation that describes light propagation. Electric field  $\bar{E} = E \hat{\varepsilon}$ , where  $\hat{\varepsilon}$  is the polarization vector, is a function of position and time, thus equation (III.31) implies four second-order derivatives in  $(\bar{x}, t)$ . Due to the coherence of the laser light, electric field  $\bar{E}$  is slowly varying in the direction of propagation over an optical wavelength. Likewise,  $\bar{E}$  is slowly varying in time over the optical period. Then, we can write the magnitude of the complex electric field in the form

$$\begin{aligned} E(\bar{x}, t) &= \alpha(\bar{x}, t) e^{i(kz - \omega t)} \\ &= |\alpha(\bar{x}, t)| e^{i\varphi(\bar{x}, t)} e^{i(kz - \omega t)}, \end{aligned} \quad (\text{III.32})$$

where  $kz - \omega t$  is the carrier wave,  $\alpha = |\alpha| e^{i\varphi}$  is the complex optical field and  $\bar{x} = (x, y, z)$ . Next, we want to substitute the electric field (III.32) into the wave equation (III.31). After taking the required derivatives, we find

$$\left[ \nabla_{\perp}^2 \alpha + \left( \frac{\partial^2 \alpha}{\partial z^2} + 2ik \frac{\partial \alpha}{\partial z} - k^2 \alpha \right) - \frac{1}{c^2} \left( \frac{\partial^2 \alpha}{\partial t^2} - 2i\omega \frac{\partial \alpha}{\partial t} - \omega^2 \alpha \right) \right] e^{i(kz - \omega t)} = 0, \quad (\text{III.33})$$

with  $\nabla_{\perp}^2 = \partial^2 / \partial x^2 + \partial^2 / \partial y^2$  the transverse Laplacian. We can simplify this equation by dropping out the second derivatives, because laser field amplitude  $|\alpha(\bar{x}, t)|$  and phase  $\varphi(\bar{x}, t)$  are slowly varying. This means that

$$\frac{\partial |\alpha|}{\partial z} = k |\alpha|, \quad \frac{\partial |\alpha|}{\partial t} = \omega |\alpha|, \quad \frac{\partial \varphi}{\partial t} = \omega \varphi \quad \text{and} \quad \frac{\partial \varphi}{\partial z} = k \varphi. \quad (\text{III.34})$$

From  $\partial|\alpha|/\partial z = k|\alpha|$  we find that  $\partial^2|\alpha|/\partial z^2 = k\partial|\alpha|/\partial z$  and similarly from  $\partial|\alpha|/\partial t = \omega|\alpha|$  we find that  $\partial^2|\alpha|/\partial t^2 = \omega\partial|\alpha|/\partial t$ , so that we are justified in dropping the second derivatives in favor of the first derivatives in (III.33). In the same equation, the last term in each parenthesis cancels out, since  $k = \omega/c \Rightarrow k^2 = \omega^2/c^2 \Rightarrow k^2\alpha = \omega^2\alpha/c^2$ . Then, after multiplying by  $e^{-i(kz-\omega t)}$ , equation (III.33) becomes

$$\left[ \nabla_{\perp}^2 + 2ik \left( \frac{\partial}{\partial z} + \frac{1}{c} \frac{\partial}{\partial t} \right) \right] \alpha(\vec{x}, t) = 0. \quad (\text{III.35})$$

In order to simplify the last expression, we introduce a new variable  $u = z - ct$  and again use the dimensionless time  $\tau = ct/L$  (where  $L$  is the propagation range). We can now rewrite the operator  $\partial/\partial z + c^{-1}\partial/\partial t$  that appears in (III.35) taking the necessary partial derivatives

$$\frac{\partial}{\partial z} = \frac{\partial u}{\partial z} \frac{\partial}{\partial u} + \frac{\partial \tau}{\partial z} \frac{\partial}{\partial \tau}, \quad (\text{III.36})$$

$$\frac{1}{c} \frac{\partial}{\partial t} = \frac{1}{c} \frac{\partial u}{\partial t} \frac{\partial}{\partial u} + \frac{1}{c} \frac{\partial \tau}{\partial t} \frac{\partial}{\partial \tau}$$

and since  $\partial u/\partial z = 1$ ,  $\partial \tau/\partial z = 0$ ,  $\partial u/\partial t = -c$  and  $\partial \tau/\partial t = c/L$ , the operator  $\partial/\partial z + c^{-1}\partial/\partial t$  is just  $L^{-1}\partial/\partial \tau$  and consequently the wave equation (III.35) is now written

$$\left( \nabla_{\perp}^2 + \frac{2ik}{L} \frac{\partial}{\partial \tau} \right) \alpha(\vec{x}, t) = 0, \quad (\text{III.37})$$

which is called the “parabolic” or “paraxial” wave equation, because we have made use of the paraxial approximations in (III.34).

At this point, it is convenient to use dimensionless transverse coordinates  $(x, y)$  along with the normalized time  $\tau$ . If we rearrange the terms in equation (III.37), we can rewrite it as

$$\left[ \left( \frac{-iL}{2k} \right) \nabla_{\perp}^2 + \frac{\partial}{\partial \tau} \right] \alpha(\tilde{x}, \tau) = 0, \quad (\text{III.38})$$

where we notice from the first term, which is the diffraction term of the wave equation, that the transverse extent of the laser beam, together with the wavenumber  $k = 2\pi/\lambda$  and the propagation range  $L$ , affect the diffraction of the beam. The equation takes a simpler form if we normalize the transverse coordinates using the relationships

$$\tilde{x} = x \left( \frac{k}{2L} \right)^{1/2}, \quad \tilde{y} = y \left( \frac{k}{2L} \right)^{1/2}. \quad (\text{III.39})$$

In (III.39), the normalization factor  $(k/2L)^{1/2}$  is related to the characteristic mode waist radius  $W_o$  by

$$W_o = \left( \frac{Z_o \lambda}{\pi} \right)^{1/2} = \left( \frac{2Z_o}{k} \right)^{1/2}, \quad (\text{III.40})$$

with  $Z_o = L$  in our case, where  $Z_o$  is the Rayleigh length, defined to be the propagation distance in which the beam doubles its area and it is determined by the curvature of the mirrors. Finally, using only dimensionless coordinates and utilizing the dimensionless transverse Laplacian, we arrive at the dimensionless parabolic wave equation, written without the tildes for convenience

$$\left( -\frac{i}{4} \nabla_{\perp}^2 + \frac{\partial}{\partial \tau} \right) \alpha(\tilde{x}, \tau) = 0. \quad (\text{III.41})$$

From this last wave equation, we notice that for a beam with transverse dimensions of the order of unity or less, we have to take into account the diffraction, since it affects the beam a great deal, over the range  $\tau = 0 \rightarrow 1$ , while for a much wider beam we can ignore it. Diffraction of the wavefront causes both the amplitude and the phase of the optical field to evolve.

### C. THE FEL WAVE EQUATION

We have found, so far, a mathematical description for the laser light that propagates in absence of sources and also for the electron motion in the presence of light. What is left, in order to generalize, is to describe the optical wave evolution, taking into account the interaction with the current source due to the electron beam. We start with the full wave equation [6]

$$\left( \nabla^2 - \frac{1}{c^2} \frac{\partial^2}{\partial t^2} \right) \vec{A}(\vec{x}, t) = -\frac{4\pi}{c} \vec{J}_\perp(\vec{x}, t), \quad (\text{III.42})$$

where  $\vec{A}(\vec{x}, t)$  is the optical vector potential and  $\vec{J}_\perp(\vec{x}, t)$  is the transverse current density due to oscillations of the electrons passing through the undulator. Then we are able to find the optical electric and magnetic fields from the vector potential using the relationships

$$\vec{E} = -\frac{1}{c} \frac{\partial \vec{A}}{\partial t}, \quad \vec{B} = \nabla \times \vec{A}. \quad (\text{III.43})$$

Once again, we will make use of the fact that laser light is coherent. Thus, we take  $\vec{A}(\vec{x}, t)$  to have a slowly varying envelope in the direction of propagation. In addition, we take the electric field to vary slowly over a laser wavelength and to vary slowly in time, relative to the optical frequency. Assuming a complex laser electric field  $E = |E|e^{i\varphi}$ , the vector potential can be written [6]

$$\vec{A}(\vec{x}, t) = \frac{E(\vec{x}, t)}{k} \hat{\varepsilon} e^{i(kz - \omega t)}, \quad (\text{III.44})$$

where  $kz - \omega t$  is the carrier wave and  $\hat{\varepsilon}$  is the laser polarization vector, which is  $\hat{\varepsilon} = (-i, 1, 0)$  for the case of a helical undulator producing circular polarized laser light. If we assume again slowly varying wave amplitude and phase and use (III.44), the wave equation (III.42) becomes

$$\begin{aligned} \frac{\hat{\varepsilon} e^{i(kz - \omega t)}}{k} \left[ \nabla_{\perp}^2 + 2ik \left( \frac{\partial}{\partial z} + \frac{1}{c} \frac{\partial}{\partial t} \right) \right] E &= -\frac{4\pi}{c} \vec{J}_{\perp} \\ \Rightarrow \left[ \nabla_{\perp}^2 + 2ik \left( \frac{\partial}{\partial z} + \frac{1}{c} \frac{\partial}{\partial t} \right) \right] E &= -\frac{4\pi k}{c} \vec{J}_{\perp} \cdot \hat{\varepsilon}^* e^{-i(kz - \omega t)}. \end{aligned} \quad (\text{III.45})$$

We will now use the same technique as we used in (III.36), introducing the new variable  $u = z - ct$  and  $\tau = ct/L$ , where  $L$  is the length of the undulator, so as to rewrite the operator  $\partial/\partial z + c^{-1} \partial/\partial t$ . Then (III.45) becomes

$$\left( \nabla_{\perp}^2 + \frac{2ik}{L} \frac{\partial}{\partial \tau} \right) E = -\frac{4\pi k}{c} \vec{J}_{\perp} \cdot \hat{\varepsilon}^* e^{-i(kz - \omega t)}. \quad (\text{III.46})$$

This last equation is the parabolic wave equation with a source current  $\vec{J}_{\perp}$ , due to the bunched electrons. The source current, which is due to all of the electrons, can be expressed as

$$\vec{J}_{\perp} = -ec \sum_i \vec{\beta}_{\perp} \delta^{(3)}(\vec{x} - \vec{r}_i(t)), \quad (\text{III.47})$$

where  $\delta^{(3)}$  is the three-dimensional Dirac delta function, defined as  $\delta^{(3)}(\vec{r}) = \delta(x)\delta(y)\delta(z)$  and  $\vec{r}_i(t)$  is the position of the  $i$ th electron at time  $t$ . The transverse velocity  $\vec{\beta}_{\perp}$  found in (III.10) can be expressed as

$$\vec{\beta}_\perp = -\frac{K}{\gamma} (\cos k_o z, \sin k_o z, 0) = \Re \left\{ -\frac{K}{\gamma} i \hat{\mathcal{E}} e^{-ik_o z} \right\}. \quad (\text{III.48})$$

Plugging (III.48) into the source current relationship in (III.47) and then the resulting source current into the parabolic wave equation (III.46), we have

$$\left( \nabla_\perp^2 + \frac{2ik}{L} \frac{\partial}{\partial \tau} \right) E = -4\pi i e K k \rho(\vec{x}, t) \langle e^{-i\zeta} / \gamma \rangle_{(\vec{x}, t)}. \quad (\text{III.49})$$

In this equation,  $\rho(\vec{x}, t)$  is the electron beam particle density in a small volume element  $dV$

$$\rho(\vec{x}, t) = \int_V \sum_i \delta^{(3)}(\vec{x} - \vec{r}_i(t)) dV, \quad (\text{III.50})$$

and with the symbol  $\langle \dots \rangle$  we denote the average over sample electrons. Employing again the dimensionless time  $\tau = ct/L$ , where  $L$  is the length of the undulator, and defining the dimensionless complex laser field  $a = |a| e^{i\varphi}$ , with the laser field amplitude  $|a| = 4\pi N e K L E / \gamma_o^2 m c^2$ , as used in (III.22), the wave equation becomes

$$\left( -\frac{iL}{2k} \nabla_\perp^2 + \frac{\partial}{\partial \tau} \right) a(\vec{x}, \tau) = - \langle j e^{-i\zeta} \rangle_{(\vec{x}, \tau)}, \quad (\text{III.51})$$

where we have introduced another important FEL parameter, the dimensionless current density  $j = 8\pi^2 N e^2 K^2 L^2 \rho / \gamma_o^3 m c^2$ , and we have made the reasonable assumption that  $\gamma \approx \gamma_o$  during the whole interaction. We want now to make the wave equation completely dimensionless, thus we bring in again the

dimensionless transverse coordinates  $\tilde{x} = x(k/2L)^{1/2}$ ,  $\tilde{y} = y(k/2L)^{1/2}$  and the dimensionless Laplacian operator. Dropping the tildes, the FEL wave equation is finally written

$$\left( -\frac{i}{4} \nabla_{\perp}^2 + \frac{\partial}{\partial \tau} \right) a(\vec{x}, \tau) = - \langle j e^{-i\zeta} \rangle_{(\vec{x}, \tau)} . \quad (\text{III.52})$$

In the case when the diffraction can be neglected, the last equation is simplified to

$$\frac{\partial a}{\partial \tau} = \overset{\circ}{a} = - j \langle e^{-i\zeta} \rangle . \quad (\text{III.53})$$

From this expression, we realize that the electron beam should be bunched, since the factor  $\langle e^{-i\zeta} \rangle$  is a measure of the electron bunching. For instance, if the electrons are bunched at around  $\zeta = \pi$ , the laser field amplitude goes up, whereas if the bunching occurs at  $\zeta = 0$ , the field amplitude goes down. Equation (III.53) also suggests that the laser field is related to the dimensionless current density  $j$ , so that when  $j \leq \pi$  we are in the low gain regime, while for  $j \gg \pi$  the coupling between the laser light and the electron beam is large and we have high gain.

#### D. GAIN

In order to better understand and describe the energy exchange between the electron and the optical beam, it is handy to make use of the gain we defined in (III.25), which is the fractional change of the optical field power during a single

pass. In terms of the optical field amplitude, gain can be written as

$$G(\tau) = \frac{|a(\tau)|^2 - a_o^2}{a_o^2} = \frac{|a(\tau)|^2}{a_o^2} - 1 \quad \text{or} \quad G(\tau) \approx 2 \left( \frac{|a(\tau)|}{a_o} - 1 \right), \quad (\text{III.54})$$

for low gain and small change in  $|a(\tau)|$  from the initial field amplitude  $a_o$ .

It is particularly useful to study the gain in the weak optical field state, because it gives us information about the performance of the FEL. For that reason, we will derive an expression for the gain, assuming weak optical fields,  $a_o = \pi$  and low gain, so as to take  $|a| \approx a_o$  and  $\varphi \approx 0$  for the whole interaction. Applying the perturbation theory, we start by expanding the electron phase  $\zeta$  and the electron phase velocity  $\nu$  in powers of the initial small field amplitude  $a_o$

$$\zeta = \zeta^{(0)} + \zeta^{(1)} + \zeta^{(2)} + \dots, \quad \overset{\circ}{\zeta} = \nu = \nu^{(0)} + \nu^{(1)} + \nu^{(2)} + \dots, \quad (\text{III.55})$$

where  $\zeta^{(0)}$  is the zeroth order in  $a_o$ ,  $\zeta^{(1)}$  is the first order, and so on. We can now plug (III.55) into the pendulum equation (III.22) to get

$$\overset{\circ\circ}{\zeta^{(0)}} + \overset{\circ\circ}{\zeta^{(1)}} + \overset{\circ\circ}{\zeta^{(2)}} + \dots = \overset{\circ}{\nu^{(0)}} + \overset{\circ}{\nu^{(1)}} + \overset{\circ}{\nu^{(2)}} + \dots = a_o \cos(\zeta^{(0)} + \zeta^{(1)} + \dots). \quad (\text{III.56})$$

From the zeroth order in  $a_o$  we have  $\overset{\circ\circ}{\zeta^{(0)}} = \overset{\circ}{\nu^{(0)}} = 0$  which gives the solutions  $\zeta^{(0)} = \zeta_o + \nu_o \tau = 0$  and  $\nu^{(0)} = \nu_o$ . From the first order in  $a_o$ , using the zeroth order solutions and integrating over time  $\tau$ , we find the solutions

$$\begin{aligned} \zeta^{(1)} &= -\frac{a_o}{\nu_o^2} \left[ \cos(\zeta_o + \nu_o \tau) - \cos(\zeta_o) + \nu_o \tau \sin(\zeta_o) \right], \\ \overset{\circ}{\nu^{(1)}} = \overset{\circ\circ}{\zeta^{(1)}} &= \frac{a_o}{\nu_o} \left[ \sin(\zeta_o + \nu_o \tau) - \sin(\zeta_o) \right]. \end{aligned} \quad (\text{III.57})$$

We can now make use of these results in the similarly expanded wave equation (III.53)

$$\overset{\circ}{a} = -j \langle e^{-i\zeta} \rangle = -j \langle e^{-i(\zeta^{(0)} + \zeta^{(1)} + \zeta^{(2)} + \dots)} \rangle. \quad (\text{III.58})$$

Taking into account only the zeroth and the first order, we can approximate the last equation

$$\overset{\circ}{a} \approx -j \langle e^{-i\zeta^{(0)}} e^{-i\zeta^{(1)}} \rangle \approx -j \langle e^{-i\zeta^{(0)}} (1 - i\zeta^{(1)}) \rangle, \quad (\text{III.59})$$

but since  $\langle e^{-i\zeta^{(0)}} \rangle = \langle e^{-i(\zeta_o + \nu_o \tau)} \rangle = \int e^{-i(\zeta_o + \nu_o \tau)} d\zeta_o / 2\pi = 0$ , (III.59) is written

$$\overset{\circ}{a} \approx j \langle e^{-i\zeta^{(0)}} i\zeta^{(1)} \rangle = ij \langle e^{-i(\zeta_o + \nu_o \tau)} \zeta^{(1)} \rangle. \quad (\text{III.60})$$

We can plug in  $\zeta^{(1)}$  from (III.57) and integrate, recalling that the complex optical field is  $a = |a| e^{i\varphi}$ , to find

$$\begin{aligned} |a(\tau)| &= a_o \left( 1 + j \left( \frac{2 - 2 \cos(\nu_o \tau) - \nu_o \tau \sin(\nu_o \tau)}{2\nu_o^3} \right) \right) + \dots, \\ \varphi(\tau) &= j \left( \frac{2 \sin(\nu_o \tau) - \nu_o \tau (1 + \cos(\nu_o \tau))}{2\nu_o^3} \right) + \dots. \end{aligned} \quad (\text{III.61})$$

Now, using equation (III.54), we are able to arrive at the low gain equation along the undulator [6]

$$G(\tau) = j \left( \frac{2 - 2 \cos(\nu_o \tau) - \nu_o \tau \sin(\nu_o \tau)}{\nu_o^3} \right). \quad (\text{III.62})$$

This equation indicates that the gain, in the weak field approximation, is proportional to the dimensionless current  $j$  and the initial electron phase velocity  $v_o$ . Plotting the final gain spectrum at  $\tau=1$  in a single pass through the undulator, as shown in Figure 9, we can verify the results we found in the phase space plots of Figures 7 and 8. Particularly, when the electrons are ejected exactly at resonance  $v_o=0$ , then there is zero net gain, meaning that the electrons lose and gain the same amount of energy during their interaction with the optical field inside the undulator. We also note, that the gain curve is anti-symmetric in  $v_o$ . The peak gain of about 13% is obtained when the FEL operates off resonance at  $v_o \approx 2.6$ , while the peak absorption occurs at  $v_o \approx -2.6$ . These results are consistent with the phase space analysis, suggesting that we must operate the FEL slightly off resonance in order to have the best exchange of energy from the electron beam to the optical mode and hence the maximum gain.

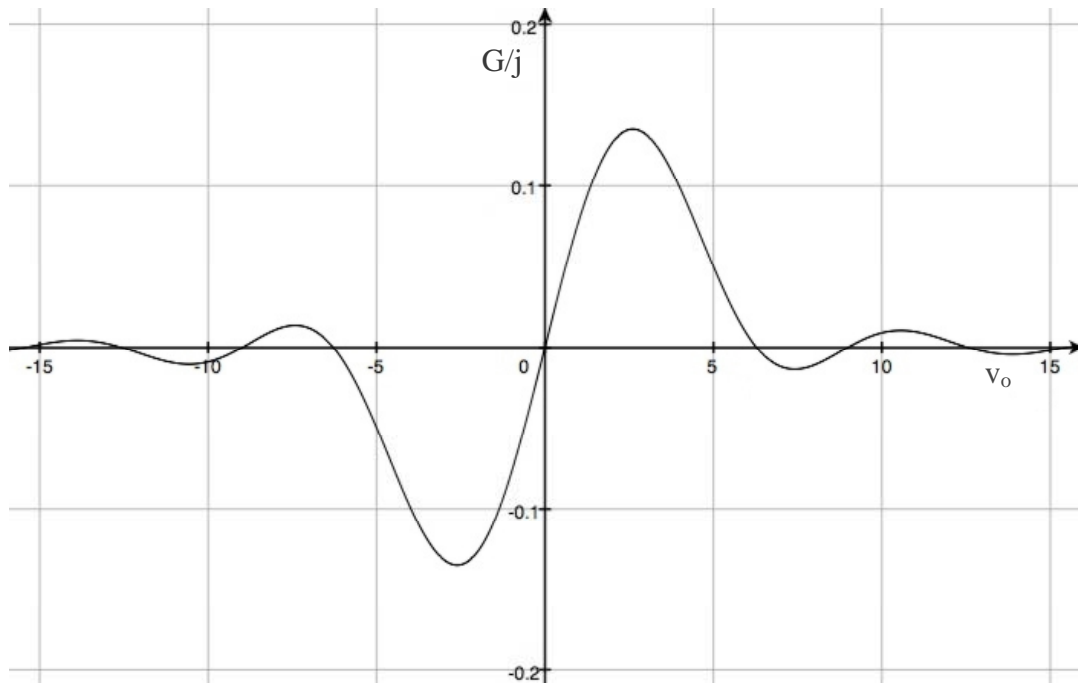


Figure 9. Single pass gain versus initial electron phase velocity  $v_o$  at  $\tau=1$ .

## IV. OPTICAL THEORY

Up to this point we have examined the interaction of the electron beam and the optical field inside the undulator, arriving at some important expressions. We have also introduced the gain  $G(\tau)$ , a useful tool to measure the performance of this interaction. In this section, we will focus our study only on the optical field, propagating in free space. Equation (III.52) describes the optical field evolution, in the more general case of the presence of source. However, when light is traveling in a sourceless medium, specifically inside the undulator while there is no electron beam present and outside the undulator, this equation reduces to equation

$$\left(-\frac{i}{4}\nabla_{\perp}^2 + \frac{\partial}{\partial\tau}\right)a(\vec{x},\tau) = 0. \quad (\text{IV.1})$$

In the following sections, we will find solutions to this wave equation, starting with the one that describes typical optical waves produced by a Free Electron Laser. We call this solution the “fundamental”, and it is the lowest-order mode. Higher-order modes, which we are going to analyze later, may also appear.

### A. FUNDAMENTAL SOLUTION TO THE WAVE EQUATION

An ideal, realizable, laser beam cross sectional shape is Gaussian. We therefore seek a Gaussian solution to the wave equation. A trial solution of this form can be written

$$a(\vec{r},\tau) = a_o p(\tau) e^{-\frac{r^2}{q(\tau)}}, \quad (\text{IV.2})$$

where  $a(\vec{r},\tau)$  is the dimensionless optical field, and  $a_o$  is the optical field amplitude at the point  $(x,y,\tau) = (0,0,0)$ ,  $r^2 = x^2 + y^2$ . The functions  $p(\tau)$  and  $q(\tau)$ ,

as yet unknown, will be determined by the wave equation (IV.1) and the initial conditions imposed by the desired Gaussian shape of the beam,

$$a(\vec{r}, 0) = a_o e^{-\frac{r^2}{z_o}}, \quad (IV.3)$$

where  $z_o = Z_o/L$  is the dimensionless Rayleigh length, and  $L$  is the propagation distance. These initial conditions give

$$p(0) = 1 \quad \text{and} \quad q(0) = z_o. \quad (IV.4)$$

In order to find the expression we are looking for, from the trial solution (IV.2), we have to find the functions  $p(\tau)$  and  $q(\tau)$ . Before putting (IV.2) into the wave equation, we switch to cylindrical coordinates, due to the symmetry of our problem. Then, the wave equation (IV.1) becomes

$$\left[ -\frac{i}{4} \frac{1}{r} \frac{\partial}{\partial r} \left( r \frac{\partial}{\partial r} \right) + \frac{\partial}{\partial \tau} \right] a(\vec{r}, \tau) = 0. \quad (IV.5)$$

Now we insert the trial solution (IV.2) into (IV.5). The first derivative of  $a(\vec{r}, \tau)$  with respect to  $r$  is

$$\frac{\partial a}{\partial r} = -2a_o r \frac{p(\tau)}{q(\tau)} e^{-\frac{r^2}{q(\tau)}}, \quad (IV.6)$$

from which

$$\frac{\partial}{\partial r} \left( r \frac{\partial a}{\partial r} \right) = 4a_o r \frac{p(\tau)}{q(\tau)} e^{-\frac{r^2}{q(\tau)}} \left( \frac{r^2}{q(\tau)} - 1 \right). \quad (IV.7)$$

Finally, we calculate the time derivative of  $a(\vec{r}, \tau)$

$$\frac{\partial a}{\partial \tau} = a_o p(\tau) e^{-\frac{r^2}{q(\tau)}} \left( \frac{1}{p(\tau)} \frac{dp}{d\tau} + \frac{r^2}{q^2(\tau)} \frac{dq}{d\tau} \right). \quad (\text{IV.8})$$

We can now go back to the wave equation (IV.5) and employ these derivatives

$$-\frac{i}{4} \frac{1}{r} \frac{\partial}{\partial r} \left( r \frac{\partial a}{\partial r} \right) + \frac{\partial a}{\partial \tau} = 0 \Rightarrow$$

$$-i a_o \frac{p(\tau)}{q(\tau)} e^{-\frac{r^2}{q(\tau)}} \left( \frac{r^2}{q(\tau)} - 1 \right) + a_o p(\tau) e^{-\frac{r^2}{q(\tau)}} \left( \frac{1}{p(\tau)} \frac{dp}{d\tau} + \frac{r^2}{q^2(\tau)} \frac{dq}{d\tau} \right) = 0. \quad (\text{IV.9})$$

Dividing through by  $a_o p(\tau) e^{-r^2/q(\tau)}$  we get

$$-i \frac{r^2}{q(\tau)} + i \frac{1}{q(\tau)} + \frac{1}{p(\tau)} \frac{dp}{d\tau} + \frac{r^2}{q^2(\tau)} \frac{dq}{d\tau} = 0. \quad (\text{IV.10})$$

Multiplying by  $-iq^2(\tau)$  and rearranging, we can write the last expression as

$$r^2 \left( -1 - i \frac{dq}{d\tau} \right) + q^2(\tau) \left( \frac{1}{q(\tau)} - \frac{i}{p(\tau)} \frac{dp}{d\tau} \right) = 0. \quad (\text{IV.11})$$

In order for this equation to hold for all  $r$  at any time  $\tau$ , the quantities in the two parentheses must be identically zero, and therefore

$$-1 - i \frac{dq}{d\tau} = 0, \quad \text{and} \quad (\text{IV.12})$$

$$\frac{1}{q(\tau)} - \frac{i}{p(\tau)} \frac{dp}{d\tau} = 0. \quad (\text{IV.13})$$

From equation (IV.12), after integrating, we find  $q(\tau) = i\tau + q_o$ , and from the initial conditions (IV.4) we see that  $q(0) = z_o$ , so that

$$q(\tau) = i\tau + z_o . \quad (IV.14)$$

Using the last result in equation (IV.13) we see that

$$\begin{aligned} \frac{dp}{d\tau} &= -\frac{ip(\tau)}{i\tau + z_o} = -\frac{p(\tau)}{-\tau + iz_o} \Rightarrow \\ \int \frac{1}{p(\tau)} dp &= \int \frac{d\tau'}{-\tau' + iz_o} \Rightarrow \\ \ln p(\tau) &= -\ln(-\tau' + iz_o) \Big|_0^\tau = -\ln(-\tau + iz_o) + \ln(iz_o) , \end{aligned} \quad (IV.15)$$

and finally

$$p(\tau) = \frac{1}{1 + i\tau/z_o} . \quad (IV.16)$$

We can now substitute  $p(\tau)$  and  $q(\tau)$  into (IV.2) and write down the solution to the parabolic wave equation as

$$a(\vec{r}, \tau) = a_o \left( \frac{1}{1 + i\tau/z_o} \right) e^{-\frac{r^2}{z_o + i\tau}} . \quad (IV.17)$$

This solution can be written in a more informative way, expressed in terms of the dimensionless beam width  $w(\tau)$ , which is defined as

$$w(\tau) = \sqrt{z_o \left( 1 + \frac{\tau^2}{z_o^2} \right)} \quad \text{or} \quad w(\tau) = \sqrt{z_o + \frac{\tau^2}{z_o}} . \quad (IV.18)$$

We note that at  $\tau = 0$ , the beam width or waist in this case (the minimum value of the beam width), is just  $w(0) = w_o = \sqrt{z_o}$ . Of course, the beam waist need not be

at the beginning of propagation distance, thus a more general expression for the beam width at any point is

$$w(\tau) = \sqrt{z_o + \frac{(\tau - \tau_w)^2}{z_o}}, \quad (\text{IV.19})$$

where  $\tau_w$  is the dimensionless position of the beam waist (normalized, as usual, to the propagation distance  $L$ ). A cross-section of a propagating Gaussian beam is shown in Figure 10. Physically, the beam width is the distance where the optical field drops to  $1/e$  of its maximum, as shown in Figure 11.

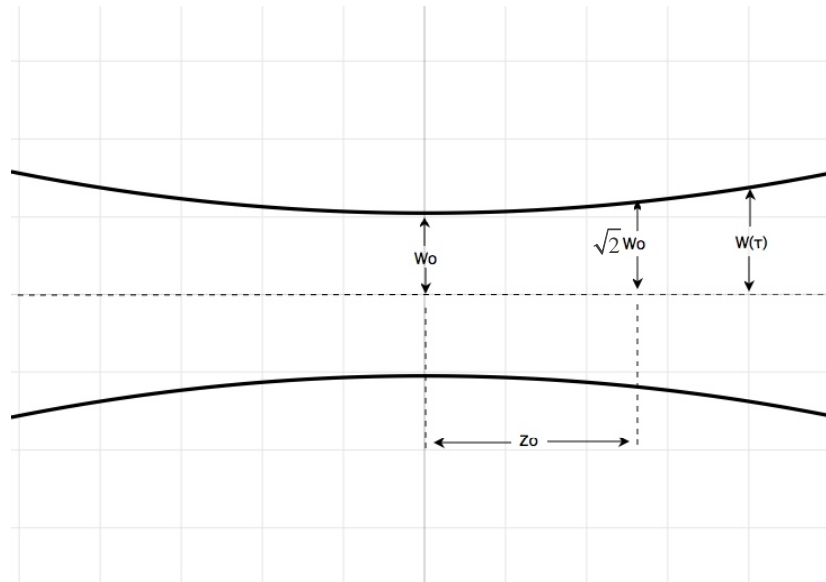


Figure 10. Cross-section of a propagating Gaussian Beam.

We are now ready to go back and modify the solution (IV.17). To make the calculations easier we let  $u = 1 + i\tau/z_o$ . Then, equation (IV.17) becomes

$$a(\vec{r}, \tau) = a_o \frac{1}{u} e^{-\frac{r^2}{z_o u}}, \quad (\text{IV.20})$$

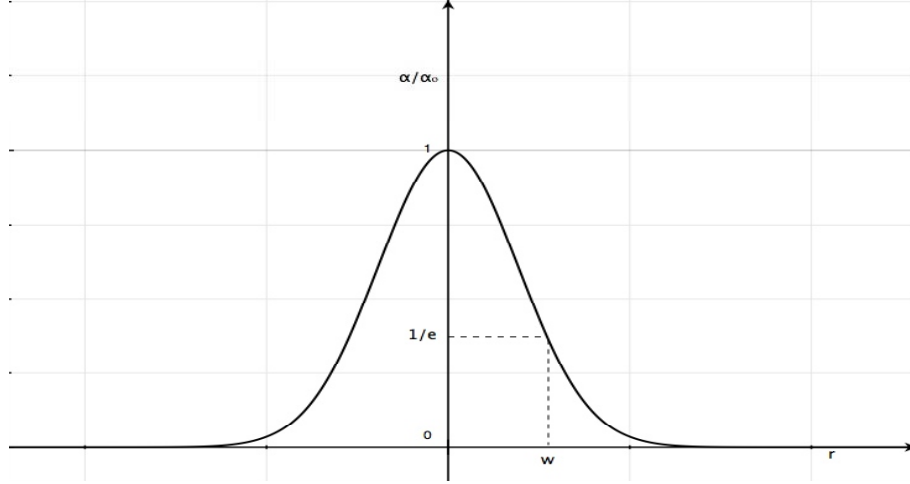


Figure 11. Gaussian beam profile.

and since the complex conjugate of  $u$  is  $u^* = 1 - i\tau/z_o$ , we can write (IV.20) as

$$\begin{aligned}
 a(\vec{r}, \tau) &= a_o \frac{1}{u} e^{-\frac{r^2 u^*}{z_o u u^*}} \Rightarrow \\
 a(\vec{r}, \tau) &= a_o \frac{1}{u} e^{-\frac{r^2 (1 - i\tau/z_o)}{z_o u u^*}} \Rightarrow \\
 a(\vec{r}, \tau) &= a_o \frac{1}{u} e^{-\frac{r^2}{z_o u u^*}} e^{\frac{i\tau r^2 / z_o}{z_o u u^*}} .
 \end{aligned} \tag{IV.21}$$

The complex number  $u$  can be written in polar form as

$$u = \sqrt{1 + \left(\frac{\tau}{z_o}\right)^2} e^{i \arctan\left(\frac{\tau}{z_o}\right)}, \tag{IV.22}$$

and since  $u u^* = 1 + (\tau/z_o)^2$ , equation (IV.21) becomes

$$\begin{aligned}
a(\vec{r}, \tau) &= a_o \frac{1}{\sqrt{1 + (\tau/z_o)^2}} e^{i \arctan(\tau/z_o)} e^{-\frac{r^2}{z_o [1 + (\tau/z_o)^2]}} e^{\frac{i \tau r^2 / z_o}{z_o [1 + (\tau/z_o)^2]}} \\
&= a_o \frac{1}{\sqrt{1 + (\tau/z_o)^2}} e^{-i \arctan(\tau/z_o)} e^{-\frac{r^2}{z_o (1 + \tau^2/z_o^2)}} e^{\frac{i \tau r^2}{z_o^2 (1 + \tau^2/z_o^2)}}.
\end{aligned} \tag{IV.23}$$

We now insert the beam width  $w(\tau)$ , defined in (IV.18), into the last equation, which becomes

$$a(\vec{r}, \tau) = a_o \frac{w_o}{w(\tau)} e^{-\frac{r^2}{w^2(\tau)}} e^{\frac{i \tau r^2}{z_o^2 + \tau^2}} e^{-i \arctan(\tau/z_o)}, \tag{IV.24}$$

where we also used  $w_o = \sqrt{z_o}$ . Finally, we can write the solution to the parabolic wave equation (IV.1) more compactly, realizing that the last two exponents in (IV.24) are pure imaginary. So, we let

$$\phi(\vec{r}, \tau) = \frac{\tau r^2}{z_o^2 + \tau^2} - \arctan\left(\frac{\tau}{z_o}\right), \tag{IV.25}$$

and write the fundamental solution as

$$a(\vec{r}, \tau) = a_o \frac{w_o}{w(\tau)} e^{-r^2/w^2(\tau)} e^{i\phi(\vec{r}, \tau)}. \tag{IV.26}$$

## B. PROPERTIES AND PROPAGATION OF GAUSSIAN BEAMS

The Gaussian beam is the lowest-order mode. A beam of this profile can be fully described by the beam waist  $w_o$  and the position of the beam waist  $\tau_w$ . We will study the behavior of the optical beams described by the solution (IV.26), in order to better understand the evolution of their properties as they propagate.

First, we note that, at the beginning of the propagation, when  $\tau = 0$ , the beam has the Gaussian shape that we chose with the initial conditions, namely

$$a(\vec{r}, 0) = a_0 e^{-\frac{r^2}{z_0}}. \quad (\text{IV.27})$$

As time increases, the beam width defined in (IV.18) gets bigger and so the transverse area of the beam expands. As a consequence, for a fixed distance from the center (fixed  $r$ ), the field strength goes down as the optical field propagates. Looking at the center of the optical mode, where  $r = 0$ , the field decreases continuously, as it is expected, since  $a(0, \tau)$  goes like  $\sim 1/\tau$ .

Gaussian modes have the very important feature that they do not change their profile as they propagate, except that the beam radius varies. In other words, a Gaussian beam stays Gaussian. This is the reason why we were looking for a solution to the wave equation of this form.

Figure 12 represents a computer simulation of the propagation of a laser light in the fundamental mode. In this figure is plotted a cross-section of the Gaussian mode as it propagates from  $\tau = 0$  to  $\tau = 1$ , together with the transverse cross-section at the beginning and at the end of the propagation distance.

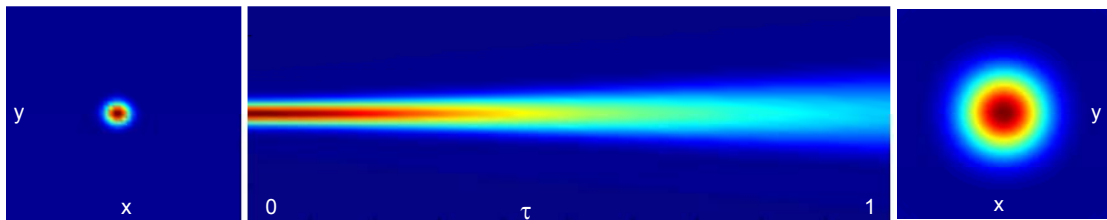


Figure 12. Cross-section of a propagating Gaussian Beam with  $\tau_w = 0$  and  $z_0 = 0.3$ .

Additionally, in Figure 13 is shown the surface plots of a Gaussian mode, at the beginning of the propagation when  $\tau = 0$ , at  $\tau = 0.5$  and at the end of the

propagation distance when  $\tau=1$  (note the difference in the vertical scale between the three graphs). From all these plots, we are able to visualize what we analyzed previously, specifically the fact that the light beam expands as it propagates and also that it suffers attenuation.

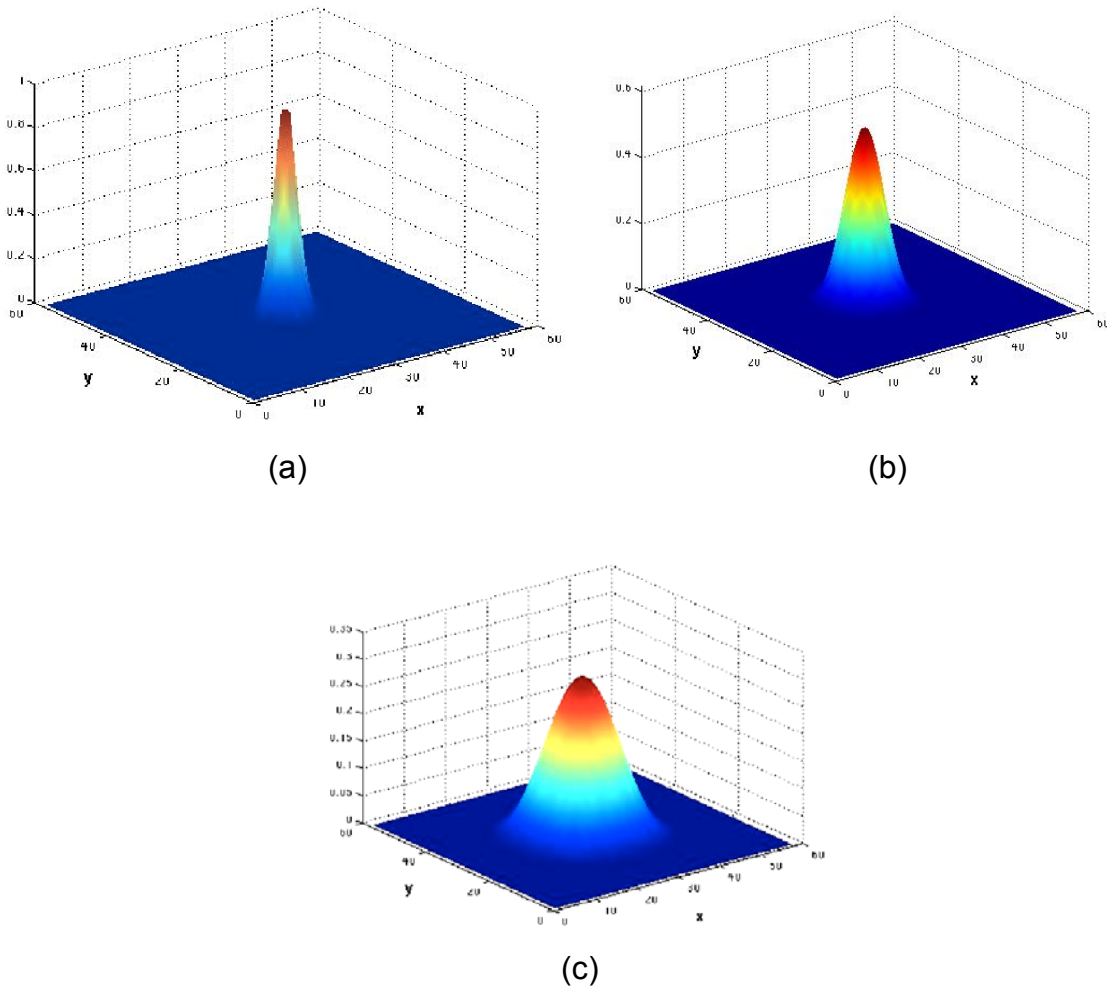


Figure 13. Surface plots of a Gaussian Beam evolution at times (a)  $\tau=0$ , (b)  $\tau=0.5$  and (c)  $\tau=1$ . Scales in z-axis are different.

THIS PAGE INTENTIONALLY LEFT BLANK

## V. HIGHER ORDER MODES

In the previous chapter, we considered only the fundamental Gaussian solution to the wave equation, which has the simplest intensity profile and is a good approximation to describe a laser beam. However, if we want to generalize for non-ideal beams and include the possible variations in the transverse beam profile, we have to find other solutions that correspond to higher order modes. These solutions to the parabolic wave equation have similar properties to the Gaussian. Furthermore, they form a complete and orthogonal set of functions, called the modes of propagation, so that every arbitrary optical beam can be expanded in terms of them [7]. We will find that the fundamental Gaussian beam is just the lowest-order mode of the generalized solution.

As one can guess, the need for studying the optical beam more extensively arises from both experimental results and simulations. Generally speaking, whenever an FEL operates under non-ideal conditions, the laser beam may contain more than one higher-order modes. Such conditions could be vibrations of the mirrors in a portable system, electron beam shifts and tilts, mirror imperfections or deformations, and so on. For instance, vibrations can cause the electron beam to be injected slightly off-axis and to deform the mirrors, while heat can change the radius of curvature and shape of the mirrors.

### A. HERMITE-GAUSSIAN MODES

The Hermite-Gaussian solutions are derived from the parabolic wave equation in rectangular coordinates, starting with the more general trial solution [8]

$$a(\vec{r}, \tau) = a_0 g\left(\frac{x}{w(\tau)}\right) h\left(\frac{y}{w(\tau)}\right) e^{-\left(p(\tau) + \frac{r^2}{z_0 q(\tau)}\right)}, \quad (\text{V.1})$$

where the functions  $p(\tau)$ ,  $q(\tau)$ ,  $g(x/w)$  and  $h(y/w)$  are found following a procedure similar to the one used for the fundamental mode. The same initial conditions as before require that

$$\begin{aligned} p(0) &= 0, & q(0) &= 1, \\ g(x/w_o) &= 1, & h(y/w_o) &= 1. \end{aligned} \tag{V.2}$$

Using (V.2) and substituting the trial solution into the wave equation, we arrive at equations that have the form of the Hermite equation and can be solved in terms of the Hermite polynomials. After finding all the four unknown functions  $p$ ,  $q$ ,  $g$  and  $h$ , we write the  $m,n$  mode of the Hermite-Gaussian beam as

$$a_{m,n}(\vec{r}, \tau) = a_o \frac{w_o}{w} H_m\left(\frac{\sqrt{2}x}{w}\right) H_n\left(\frac{\sqrt{2}y}{w}\right) e^{-r^2/w^2} e^{i\phi_{m,n}(\vec{r}, \tau)}, \tag{V.3}$$

where the phase is

$$\phi_{m,n}(\vec{r}, \tau) = \frac{r^2 \tau}{w_o^2 w^2} - (m+n+1) \arctan\left(\frac{\tau}{z_o}\right), \tag{V.4}$$

and  $m, n$  are positive integers identifying the mode. In (V.3),  $H_m$  and  $H_n$  are the Hermite polynomials with  $m, n$  the non-negative integer indices. These indices determine the shape of the beam profile in the x and y direction respectively. The first ten of the Hermite polynomials are listed in Table 1. It is obvious that when  $m=0$  and  $n=0$ , the Hermite-Gaussian beam is just the Gaussian beam, which is why it is called the fundamental mode. A few examples of higher order Hermite-Gaussian modes are shown in Figure 14, where we note that  $m$  nodes appear running vertically, while  $n$  nodes run horizontally.

$H_0(u) = 1$
$H_1(u) = 2u$
$H_2(u) = 4u^2 - 2$
$H_3(u) = 8u^3 - 12u$
$H_4(u) = 16u^4 - 48u^2 + 12$
$H_5(u) = 32u^5 - 160u^3 + 120u$
$H_6(u) = 64u^6 - 480u^4 + 720u^2 - 120$
$H_7(u) = 128u^7 - 1344u^5 + 3360u^3 - 1680u$
$H_8(u) = 256u^8 - 3584u^6 + 13440u^4 - 13440u^2 + 1680$
$H_9(u) = 512u^9 - 9216u^7 + 48384u^5 - 80640u^3 + 30240u$

Table 1. Hermite polynomials

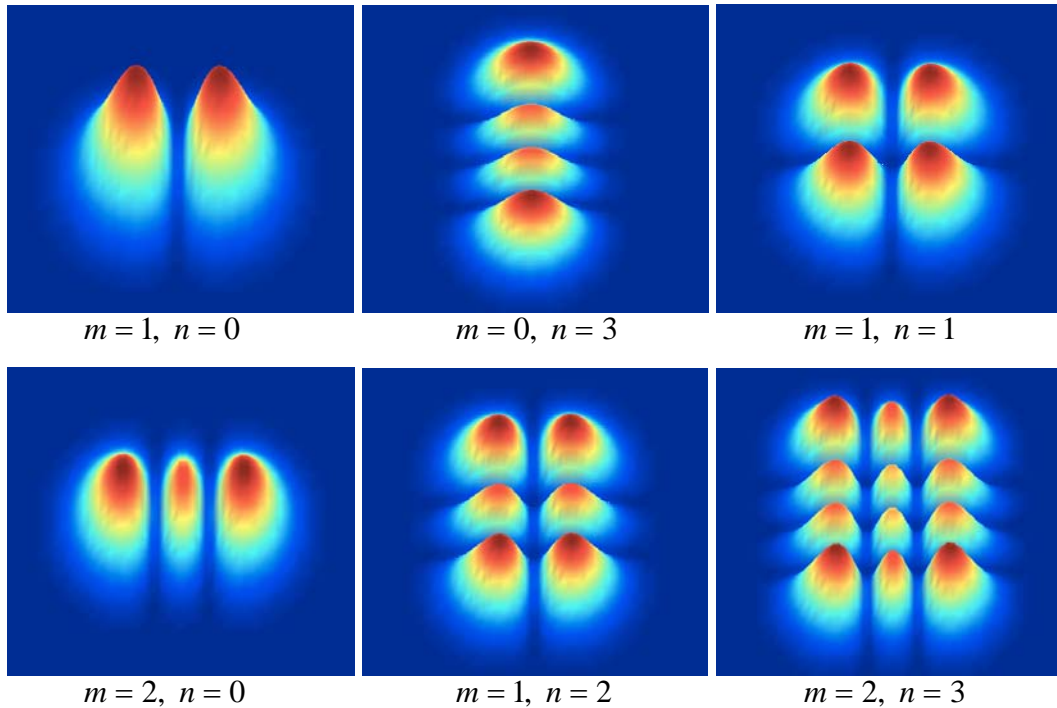


Figure 14. Hermite-Gaussian modes in the transverse plane  $x, y$ . Red indicates highest intensity, while blue indicates least intensity.

## B. LAGUERRE-GAUSSIAN MODES

The optical cavity of an FEL, utilizing circular mirrors and a round, aligned electron beam, has cylindrical symmetry. This fact suggests that we should use cylindrical coordinates to solve the dimensionless parabolic wave equation (IV.1), which is now written

$$\frac{\partial^2 \mathbf{a}}{\partial r^2} + \frac{1}{r} \frac{\partial \mathbf{a}}{\partial r} + \frac{1}{r^2} \frac{\partial^2 \mathbf{a}}{\partial \vartheta^2} + 4i \frac{\partial \mathbf{a}}{\partial \tau} = 0, \quad (\text{V.5})$$

since the dimensionless transverse Laplacian in cylindrical coordinates is

$$\nabla_{\perp}^2 = \frac{\partial^2}{\partial r^2} + \frac{1}{r} \frac{\partial}{\partial r} + \frac{1}{r^2} \frac{\partial^2}{\partial \vartheta^2}. \quad (\text{V.6})$$

Motivated from the success in finding the Hermite-Gaussian modes trying the solution (V.1), we will now put a similar exponential term in the trial solution for the wave equation, adding  $e^{il\vartheta}$  to match the single valued periodic boundary conditions, where  $l$  is an integer. We also guess a power series in  $r$ , and since we anticipate diffraction that suggests the use of  $r/w$  dependence, we try the solution

$$\mathbf{a}(\vec{r}, \vartheta, \tau) = \mathbf{a}_o \left( \frac{\sqrt{2} r}{w(\tau)} \right)^l \ell \left( \frac{2r^2}{w^2(\tau)} \right) e^{-\left( P(\tau) + \frac{r^2}{z_o q(\tau)} - il\vartheta \right)}, \quad (\text{V.7})$$

where  $\ell(2r^2/w^2)$ ,  $P(\tau)$  and  $q(\tau)$  are the unknown functions that we will try to find next. Although we use cylindrical coordinates, we still require that at  $\tau = 0$

$$\mathbf{a}(\vec{r}, \vartheta, 0) = \mathbf{a}_o e^{-\frac{r^2}{z_o}} e^{il\vartheta}, \quad (\text{V.8})$$

which gives  $\ell(2r^2/w^2)=1$ ,  $P(0)=0$  and  $q(0)=1$ . In order to put the trial solution (V.7) into the wave equation (V.5), we first need to calculate the derivatives of the function  $\ell(2r^2/w^2)$  using the chain rule

$$\frac{\partial \ell(2r^2/w^2)}{\partial r} = \frac{\partial \ell(2r^2/w^2)}{\partial (2r^2/w^2)} \frac{\partial (2r^2/w^2)}{\partial r} = \frac{4r}{w^2} \ell', \quad (\text{V.9})$$

where we used the prime to represent the first derivative of  $\ell$  with respect to its argument  $2r^2/w^2$ . Similarly, using the double prime for the second derivative, we find

$$\frac{\partial^2 \ell(2r^2/w^2)}{\partial r^2} = \frac{\partial}{\partial r} \left( \frac{4r}{w^2} \ell' \right) = \frac{4}{w^2} \left( \ell' + r \frac{\partial \ell'}{\partial r} \right) = \frac{4\ell'}{w^2} + \frac{16r^2}{w^4} \ell''. \quad (\text{V.10})$$

The time derivative of  $\ell(2r^2/w^2)$  is

$$\frac{\partial \ell(2r^2/w^2)}{\partial \tau} = \frac{\partial \ell(2r^2/w^2)}{\partial (2r^2/w^2)} \frac{\partial (2r^2/w^2)}{\partial \tau} = \ell'(2r^2) \frac{\partial (1/w^2)}{\partial \tau} = -\frac{4r^2 \dot{w}}{w^3} \ell', \quad (\text{V.11})$$

with  $(\dot{\phantom{x}})$  indicating the derivative with respect to the dimensionless time  $\tau$ . Now we are ready to calculate the derivatives of the trial solution (V.7)

$$\frac{\partial \mathbf{a}}{\partial r} = \mathbf{a}_o \left( \frac{\sqrt{2}}{w} \right)^l e^{-\left( P + \frac{r^2}{z_o q} - i l g \right)} \left[ l \ell r^{l-1} + \frac{4r^{l+1}}{w^2} \ell' - \frac{2r^{l+1}}{z_o q} \ell \right], \quad (\text{V.12})$$

$$\begin{aligned} \frac{\partial^2 \mathbf{a}}{\partial r^2} = \mathbf{a}_o \left( \frac{\sqrt{2}}{w} \right)^l e^{-\left( P + \frac{r^2}{z_o q} - i l g \right)} & \left[ \frac{16r^{l+2}}{w^4} \ell'' + \left( \frac{8lr^l}{w^2} - \frac{16r^{l+2}}{w^2 z_o q} + \frac{4r^l}{w^2} \right) \ell' + \right. \\ & \left. + \left( \frac{4r^{l+2}}{z_o^2 q^2} - \frac{4lr^l}{z_o q} - \frac{2r^l}{z_o q} + l^2 r^{l-2} - lr^{l-2} \right) \ell \right], \quad (\text{V.13}) \end{aligned}$$

$$\frac{\partial \mathbf{a}}{\partial \tau} = \mathbf{a}_o \left( \frac{\sqrt{2}}{w} \right)^l e^{-\left( P + \frac{r^2}{z_o q} - il\vartheta \right)} \left[ -\frac{4 \dot{w} r^{l+2}}{w^3} \ell' + \left( \frac{r^{l+2} \dot{q}}{z_o q^2} - \frac{l \dot{w} r^l}{w} - r^l \dot{P} \right) \ell \right], \quad (\text{V.14})$$

$$\frac{\partial \mathbf{a}}{\partial \vartheta} = i \mathbf{a}_o l \left( \frac{\sqrt{2} r}{w} \right)^l \ell e^{-\left( P + \frac{r^2}{z_o q} - il\vartheta \right)}, \quad (\text{V.15})$$

$$\frac{\partial^2 \mathbf{a}}{\partial \vartheta^2} = -\mathbf{a}_o l^2 \left( \frac{\sqrt{2} r}{w} \right)^l \ell e^{-\left( P + \frac{r^2}{z_o q} - il\vartheta \right)}. \quad (\text{V.16})$$

Next, we want to substitute the trial solution (V.7) into the wave equation (V.5).

Bringing all the derivatives together and dividing through by  $\mathbf{a}_o \left( \sqrt{2}/w \right)^l e^{-\left( P + \frac{r^2}{z_o q} - il\vartheta \right)}$

we have

$$\begin{aligned} \frac{\partial^2 \mathbf{a}}{\partial r^2} + \frac{1}{r} \frac{\partial \mathbf{a}}{\partial r} + \frac{1}{r^2} \frac{\partial^2 \mathbf{a}}{\partial \vartheta^2} + 4i \frac{\partial \mathbf{a}}{\partial \tau} = 0 \Rightarrow \\ \frac{16 r^{l+2}}{w^4} \ell'' + \left( \frac{8 l r^l}{w^2} - \frac{16 r^{l+2}}{w^2 z_o q} + \frac{4 r^l}{w^2} - \frac{16 i \dot{w} r^{l+2}}{w^3} \frac{4 r^l}{w^2} \right) \ell' + \left( \frac{4 r^{l+2}}{z_o^2 q^2} - \frac{4 l r^l}{z_o q} - \frac{2 r^l}{z_o q} + \right. \\ \left. + l^2 r^{l-2} - l r^{l-2} + l r^{l-2} - \frac{2 r^l}{z_o q} - l^2 r^{l-2} + \frac{4 i r^{l+2} \dot{q}}{z_o q^2} - \frac{4 i l \dot{w} r^l}{w} - 4 i r^l \dot{P} \right) \ell = 0 \Rightarrow \\ \underbrace{\frac{4 r^2 \ell''}{w^4} + \frac{2 l \ell'}{w^2} - \frac{4 r^2 \ell'}{w^2 z_o q} + \frac{2 \ell'}{w^2} - \frac{4 i \dot{w} r^2 \ell'}{w^3}}_{r \text{ and } \ell \text{ dependence}} + \underbrace{\frac{r^2}{z_o^2 q^2} + \frac{i r^2 \dot{q}}{z_o q^2}}_{\text{only } r^2 \text{ dependence}} - \underbrace{\frac{l+1}{z_o q} - \frac{i l \dot{w}}{w} - i \dot{P}}_{\text{no } r \text{ dependence}} = 0. \quad (\text{V.17}) \end{aligned}$$

We want this equation to have solutions for each transverse plane, or in other words, for each fixed time  $\tau$ . Thus, we need to set the  $r$  and  $\ell$  dependent terms equal to a constant, while the  $r^2$  dependent terms should be equal to zero because equation (V.17) must be valid for any transverse position. Eventually, the terms with no  $r$  dependence must be equal and opposite to the constant

value of the terms dependent on  $r$  and  $\ell$ , in order for the equality to be true. Hence, we have to solve the following three equations simultaneously

$$\frac{4r^2}{w^4} \frac{\ell''}{\ell} + \frac{2l}{w^2} \frac{\ell'}{\ell} - \frac{4r^2}{w^2 z_o q} \frac{\ell'}{\ell} + \frac{2}{w^2} \frac{\ell'}{\ell} - \frac{4i \overset{\circ}{w} r^2}{w^3} \frac{\ell'}{\ell} = -\xi, \quad (\text{V.18})$$

$$\frac{r^2}{z_o^2 q^2} + \frac{i r^2 \overset{\circ}{q}}{z_o q^2} = 0, \quad (\text{V.19})$$

$$-\frac{l+1}{z_o q} - \frac{i l \overset{\circ}{w}}{w} - i \overset{\circ}{P} = \xi, \quad (\text{V.20})$$

where we used  $-\xi$  as the constant for the  $r$  and  $\ell$  dependent terms. We will start from (V.19), since it is straightforward

$$\frac{r^2}{z_o^2 q^2} + \frac{i r^2 \overset{\circ}{q}}{z_o q^2} = 0 \Rightarrow \frac{r^2}{z_o q^2} \left( \frac{1}{z_o} + i \overset{\circ}{q} \right) = 0 \Rightarrow \frac{1}{z_o} + i \overset{\circ}{q} = 0, \quad (\text{V.21})$$

where for the last step we use the same argument as we did for the derivation of the fundamental mode, namely that the equation must hold for all  $r$ . After integrating, and since  $q(0) = 1$  from the initial conditions, we find

$$q(\tau) = \frac{i \tau}{z_o} + 1. \quad (\text{V.22})$$

From the definition of the beam width  $w(\tau) = \sqrt{z_o + \tau^2/z_o}$  in (IV.18), we have  $\overset{\circ}{w} = \tau/wz_o$ . Rearranging terms in equation (V.18) we write

$$\ell'' + \left( \frac{w^2 l}{2r^2} - \frac{w^2}{z_o q} + \frac{w^2}{2r^2} + \frac{i \tau}{z_o} \right) \ell' + \frac{w^4 \xi}{4r^2} \ell = 0, \quad (\text{V.23})$$

where the terms in the parenthesis, after substituting  $q(\tau)$  from (V.22) and using  $z_o = w_o^2$ , become

$$\frac{w^2 l}{2r^2} - \frac{w^2}{z_o q} + \frac{w^2}{2r^2} + \frac{i \tau}{z_o} = \frac{w^2 l}{2r^2} - 1 + \frac{w^2}{2r^2}. \quad (\text{V.24})$$

Let  $u = 2r^2/w^2$  to rewrite (V.23) more compactly as

$$u |'' + (l+1-u) |' + \frac{\xi w^2}{2} | = 0, \quad (\text{V.25})$$

which has the form  $xy'' + (l+1-x)y' + py = 0$ , of the differential equation for the associated Laguerre function [9], where  $l$  and  $p$  are real numbers. When  $p$  is a non-negative integer, i.e.  $p = 0, 1, 2, 3, \dots$ . Laguerre differential equation has as solutions the associated Laguerre polynomials  $L_p^l(x)$ . The first few polynomials are listed in Table 2.

$L_0^l(x) = 1$ $L_1^l(x) = -x + l + 1$ $L_2^l(x) = \frac{1}{2} [x^2 - 2(l+2)x + (l+1)(l+2)]$ $L_3^l(x) = \frac{1}{6} [-x^3 + 3(l+3)x^2 - (l+2)(l+3)x + (l+1)(l+2)(l+3)]$
--

Table 2. Associated Laguerre polynomials From [9].

From equation (V.25), the Laguerre polynomials specify the constant  $\xi$  as

$$\frac{\xi w^2}{2} = p \quad \text{so that} \quad \xi = \frac{2p}{w^2}. \quad (\text{V.26})$$

We can now use this result in the equation (V.20) in order to find the last unknown function  $P(\tau)$

$$-\frac{l+1}{z_o q} - \frac{i l w}{w} - i \overset{\circ}{P} = \frac{2p}{w^2} \Rightarrow \overset{\circ}{P} = \frac{i l}{z_o q} + \frac{i}{z_o q} - \frac{l \tau}{w^2 z_o} + \frac{2i p}{w^2}. \quad (\text{V.27})$$

We rewrite the last equation, using  $q(\tau)$  from (V.22) and  $w^2 = z_o + \tau^2/z_o$ , so that

$$\overset{\circ}{P} = i z_o (1+l+2p) \frac{1}{z_o^2 + \tau^2} + \frac{\tau}{z_o^2 + \tau^2}. \quad (\text{V.28})$$

Finally, integration from 0 to  $\tau$  gives

$$P(\tau) = i (1+l+2p) \arctan\left(\frac{\tau}{z_o}\right) + \frac{1}{2} \ln\left(\frac{z_o^2 + \tau^2}{z_o^2}\right). \quad (\text{V.29})$$

At this point, we have found all the unknown functions  $P(\tau)$ ,  $q(\tau)$  and power series  $L_p^l$  and we can put them into the trial solution (V.7). After rearranging terms, we can write down the solution to the parabolic wave equation of the  $(p, l)$  mode. This solution is usually referred as the  $(p, l)$  Laguerre-Gaussian mode

$$a_{p,l}(\vec{r}, \vartheta, \tau) = a_o \frac{w_o}{w} \left(\frac{\sqrt{2} r}{w}\right)^l L_p^l\left(\frac{2r^2}{w^2}\right) e^{-\frac{r^2}{w^2}} e^{i \phi_p^l(\vec{r}, \vartheta, \tau)}, \quad (\text{V.30})$$

with phase

$$\phi_p^l(\vec{r}, \vartheta, \tau) = -(1+l+2p) \arctan\left(\frac{\tau}{z_o}\right) + \frac{r^2 \tau}{z_o^2 + \tau^2} + l \vartheta. \quad (\text{V.31})$$

and the Laguerre polynomials listed in Table 2.

## C. LAGUERRE-GAUSSIAN MODE ANALYSIS

### 1. Intensity Plots

Solving the parabolic wave equation in cylindrical coordinates, we find a family of modes, in equation (V.30), that are expressed in terms of the product of a Gaussian envelope, a Laguerre polynomial and a phase term. Each mode is of the  $(p, l)$  order, where  $p$  is the radial mode number and  $l$  is the angular mode number. For this reason, the Laguerre-Gaussian modes are usually denoted as  $LG_p^l$  modes.

Figure 15 shows the intensity profiles of various  $LG_p^l$  modes at  $\tau = 0$ , created from simulations using C code. In these plots there is no phase information displayed, since we are plotting the  $a_{p,l} \times a_{p,l}^*$  quantity. Examining these plots, we are able to evaluate several features of the Laguerre-Gaussian beams.

We see that the lowest order mode  $LG_0^0$  is just the fundamental Gaussian mode, as expected. The other modes, with  $p = 0$  and  $l > 0$ , have a simple ring profile, since they have one central node. As the angular mode number  $l$  increases, the central, near-zero intensity region becomes larger, which is also true for modes with  $p > 0$ . All modes with  $p > 0$  have a profile in the form of concentric rings. The radial mode number  $p$  indicates the number of nodes and therefore the number of the rings. Thus, the total number of dark nodes is  $p$  at  $r \neq 0$ , in addition to the central node. These  $p + 1$  nodes come from the zeros of the Laguerre polynomials. We also see that the width of the rings gets narrower for beams with higher  $l$  and same  $p$ . Finally, as the radial mode number  $p$  increases, the effective width of the beam gets bigger.

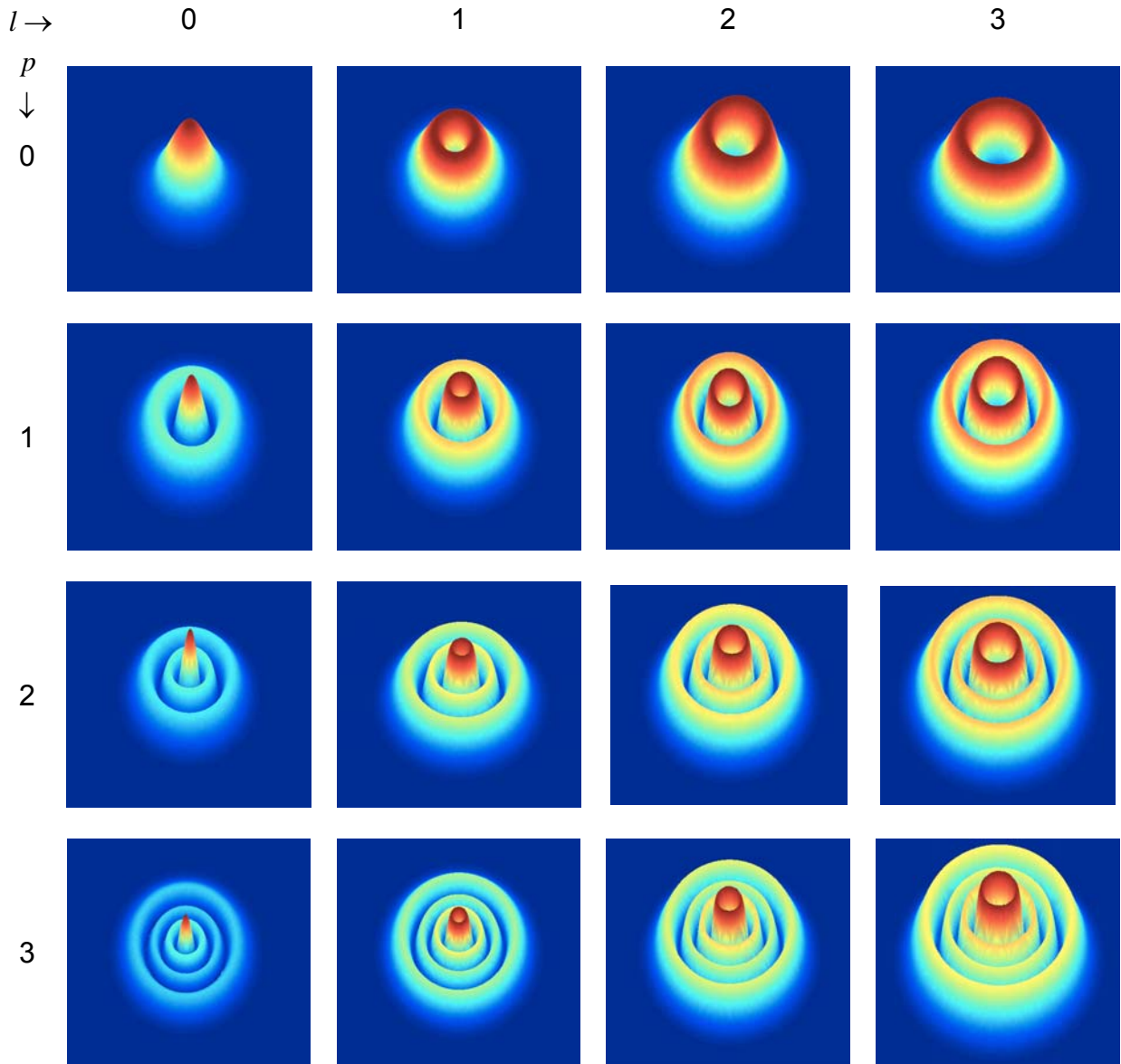


Figure 15. Laguerre-Gaussian modes  $LG_p^l$  ; Intensity plots ( $a_{p,l} \times a_{p,l}^*$ ) in the transverse plane  $x, y$ , at  $\tau = 0$ , where red is most intense, while blue is least intense.

In order to see more clearly how an  $LG_p^l$  beam varies along the transverse plane, we plot in Figure 16 for two sample modes, the radial intensity distribution of the Laguerre-Gaussian beam across a diametric plane.

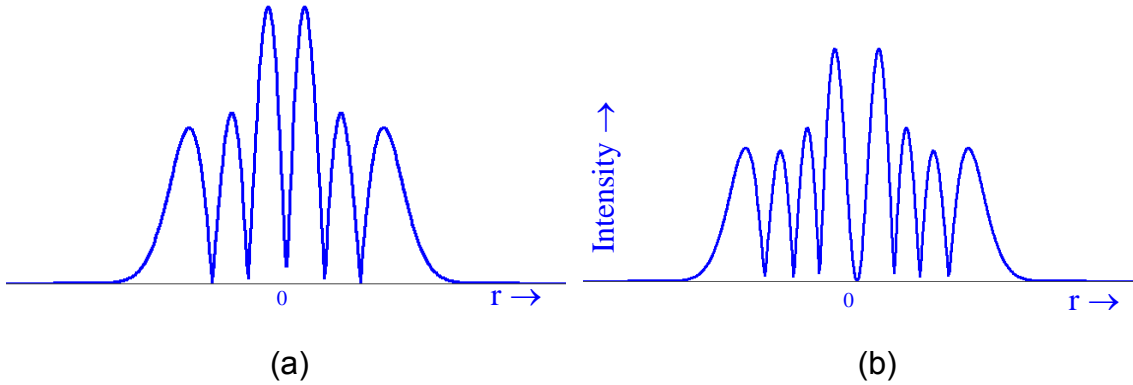


Figure 16. Radial intensity distribution for (a)  $LG_2^1$  and (b)  $LG_3^2$  beams.

## 2. Plots of Real Part

Plotting only the intensity of a Laguerre-Gaussian mode, we neglect phase. These effects turn out to play an important role in the evolution of a propagating beam. In Figure 17, we plot the same Laguerre-Gaussian modes as in Figure 15, but this time we include the phase term of equation (V.30) by plotting the real part squared. We could as well plot the real part, but in this case we would have to plot negative values of the optical field amplitude  $a$ . We immediately note that in all modes, except for the fundamental  $LG_0^0$ , radial nodes appear. The number of nodes is proportional to the angular mode number  $l$ , since when  $\tau = 0$ , the phase (V.31) is just  $\phi_p^l(\vec{r}, \vartheta, \tau) = l\vartheta$ .

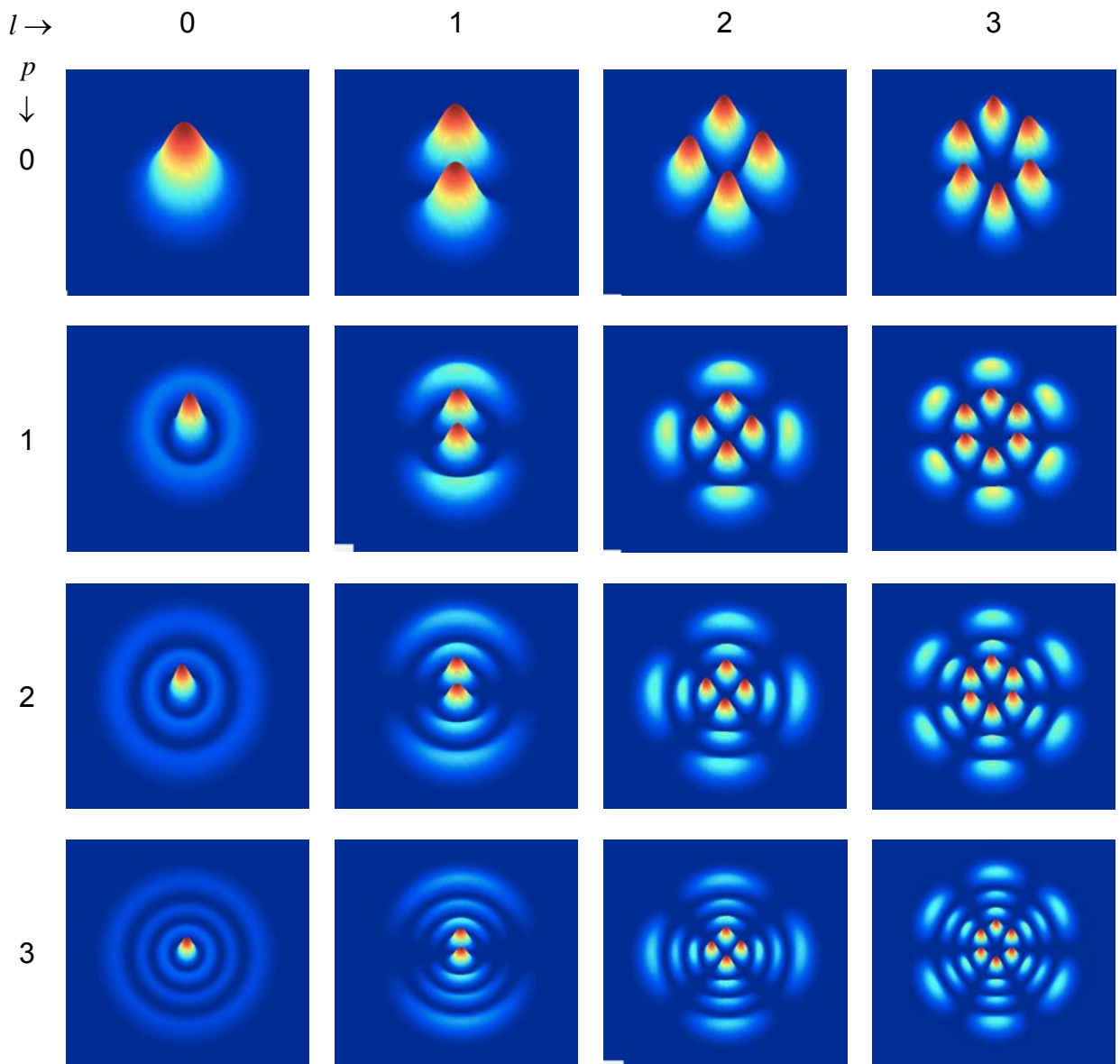


Figure 17. Laguerre-Gaussian modes  $LG_p^l$  ; plots of the real part squared, at  $\tau = 0$ .

## D. PROPAGATION OF LAGUERRE-GAUSSIAN MODES

We have seen previously in Figure 12 that a Gaussian beam, which is an  $LG_0^0$  beam, retains its shape as it propagates. We find, by running similar simulations, that this is true for all higher-order modes, provided the laser beam consists of only one pure mode.

### 1. Intensity Plots

Figure 18 shows the results of computer simulations for the evolution of several Laguerre-Gaussian modes as they propagate from  $\tau=0$  to  $\tau=1$ . We show the intensity plots of the transverse cross section at the beginning and at the end of the propagation, and the cross section of the beam from  $\tau=0$  to  $\tau=1$ . It is clear that as the beam evolves, its shape is unchanged. The central node is preserved, and even though the beam diverges, the multiple radial nodes persist. Nevertheless, we can see clearly that the peak intensities of the rings (antinodes) decrease as a function of the propagation distance, showing that the beam spreads reducing intensity.

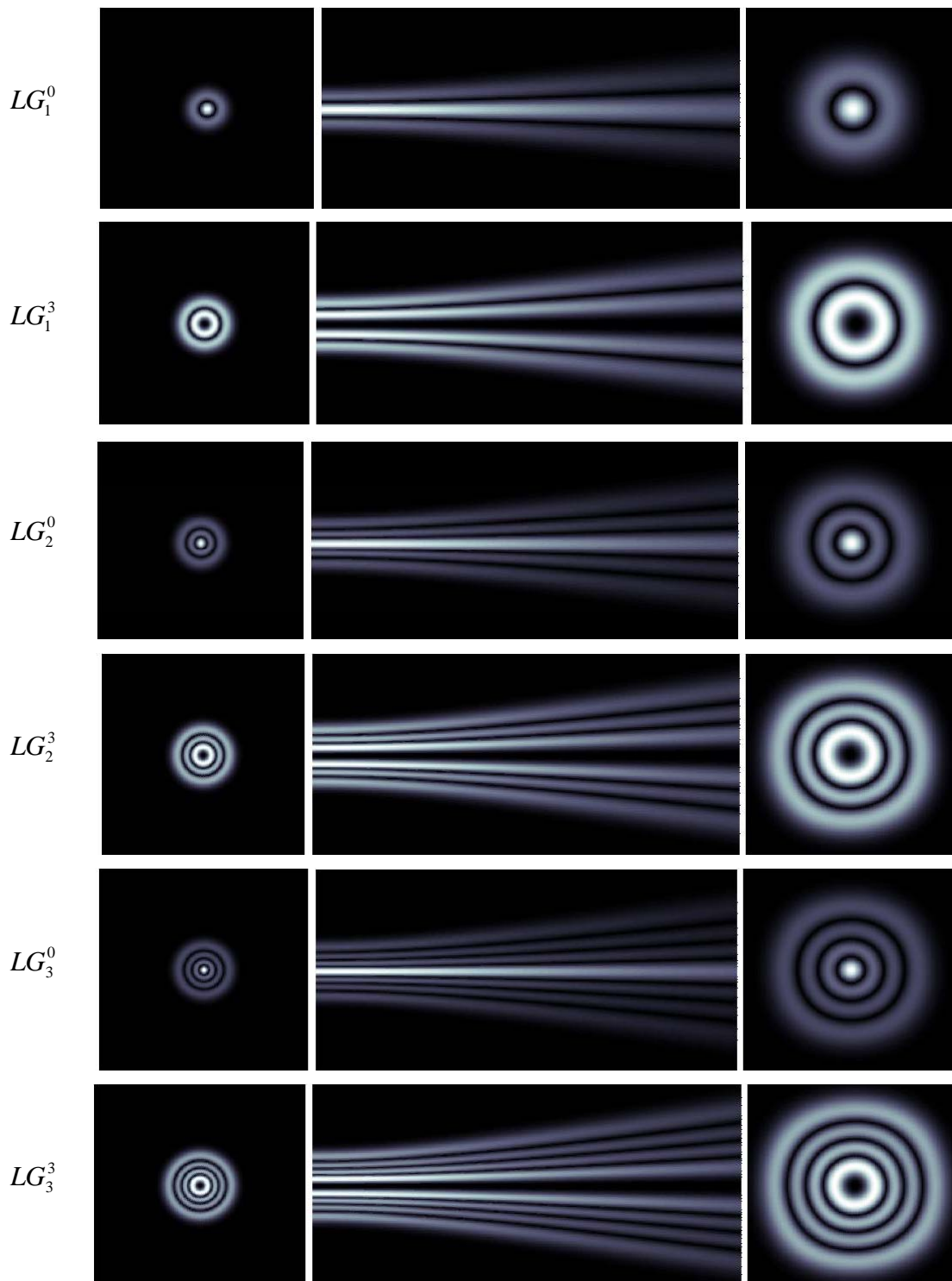


Figure 18. Intensity plots of Laguerre-Gaussian modes as they propagate.

## 2. Plots of Real Part

In order to complete our study of the evolution of the Laguerre-Gaussian beams, we must examine the phase structure of the beam as it propagates. Simulations have shown that we have to take into account the well-known fact that light carries angular momentum [10]. For example, in the case of a circularly polarized beam, light carries an angular momentum that relates to the spin of individual photons. Furthermore, a light beam can also have orbital angular momentum, a feature that can be deduced classically from Maxwell's equations. It has been shown that for a Laguerre-Gaussian beam, the orbital angular momentum is well defined and has a value of  $lh$  per photon, where  $l$  is the angular mode number and  $h$  is the Planck's constant [11].

The orbital angular momentum arises from the azimuthal dependence, particularly from the term  $e^{il\vartheta}$  of the solution to the wave equation (V.30). We will analyze this solution a bit more by examining a sample of Laguerre-Gaussian beams. We will plot the real part of the solution (V.30), so as to include the phase and see how it changes along the propagation distance. In the following figures we show the surface plots of a few Laguerre-Gaussian modes at the end of the propagation distance (where  $\tau=1$ ). In this way, we can see how the phases evolve, compared to their initial shapes at  $\tau=0$ , presented in Figure 17. For each mode we plot the real part and the real part squared, so that in the latter we avoid plotting negative values, as we did in Figure 17.

Starting with the  $LG_0^3$  mode, we put  $\tau=1$  in the solution (V.30) and we use Table 2 to find the associated Laguerre polynomial with  $p=0$ . Then, the real part of the solution can be written explicitly as

$$a_{0,3}(\vec{r}, \vartheta, 1) = a_0 \frac{2^{3/2} z_0^{5/2}}{(z_0^2 + 1)^2} r^3 e^{-\frac{r^2 z_0}{z_0^2 + 1}} \cos \left[ \frac{r^2}{z_0^2 + 1} - 4 \arctan \left( \frac{1}{z_0} \right) + 3\vartheta \right]. \quad (\text{V.32})$$

Figure 19 shows two surface plots at time  $\tau = 1$ , for a  $LG_0^3$  laser mode. In Figure 19(a) we plot the real part, as described by equation (V.32), while in Figure 19(b) we plot the real part squared. We notice that a spiral pattern appears in the mode structure, due to the fact that the phase rotates as a function of  $r$  and the angle  $\vartheta$ . We have to stress that the light does not follow a spiral path; it is just the phase that changes in a way that it describes such a spiral path. This path, in three dimensions is somewhat helical [10].

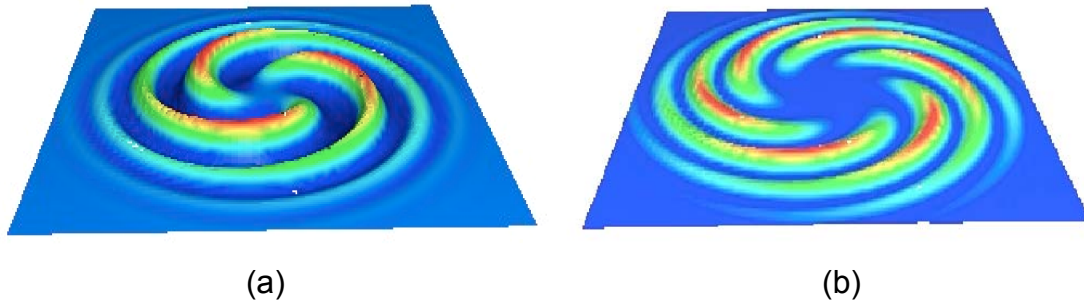


Figure 19. Plots of (a) real part and (b) real part squared of a  $LG_0^3$  beam at the end of the propagation distance ( $\tau = 1$ ), with  $a_o = 1$  and  $z_o = 0.4$ .

Other examples of the evolution of Laguerre-Gaussian beams, including phase change, are shown in Figure 20 and Figure 21, where we present, as in Figure 19, the surface plots of a  $LG_1^2$  and a  $LG_2^1$  laser beam respectively.

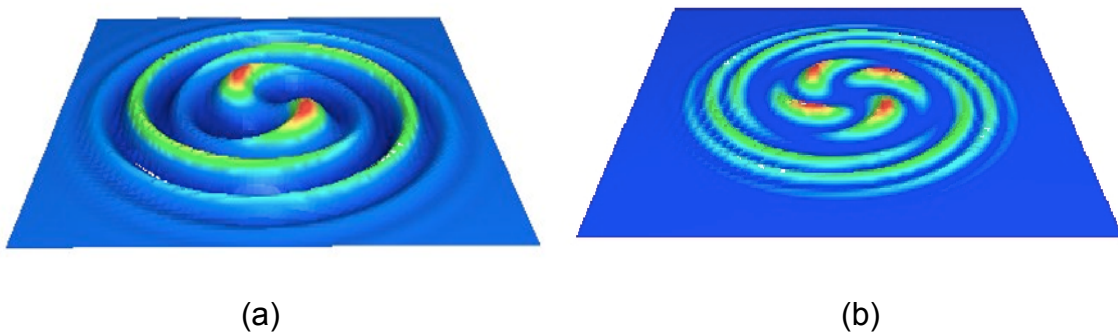


Figure 20. Plots of (a) real part and (b) real part squared of a  $LG_1^2$  beam at the end of the propagation distance ( $\tau = 1$ ), with  $a_o = 1$  and  $z_o = 0.4$ .

The solution to the parabolic wave equation for the  $LG_2^1$  mode can be written in more detail as

$$a_{2,1}(\vec{r}, \vartheta, 1) = a_o \frac{\sqrt{2} z_o^{5/2}}{z_o^2 + 1} \left[ \frac{2z_o^2 r^5}{(z_o^2 + 1)^2} - \frac{6z_o r^3}{z_o^2 + 1} + 3r \right] e^{\frac{r^2 z_o}{z_o^2 + 1}} \cos \left[ \frac{r^2}{z_o^2 + 1} - 6 \arctan \left( \frac{1}{z_o} \right) + \vartheta \right], \quad (\text{V.33})$$

giving the plots of Figure 21. We observe again the spiral patterns due to the phase evolution. We can see more clearly how  $a_{\text{real}}$  varies with  $r$  in Figure 22, where we show the radial distribution of  $a_{\text{real}}$  along various angles.

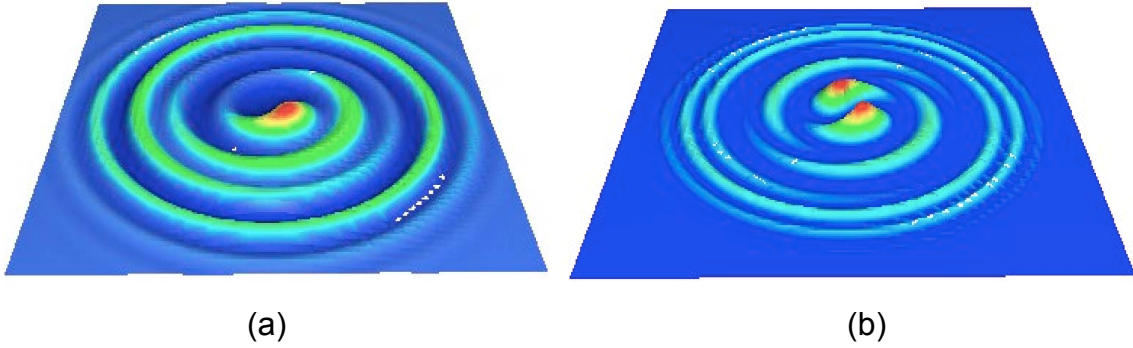


Figure 21. Plots of (a) real part and (b) real part squared of a  $LG_2^1$  beam at the end of the propagation distance ( $\tau = 1$ ), with  $a_o = 1$  and  $z_o = 0.4$ .

Analyzing equation (V.33), we recognize the term  $e^{\frac{r^2 z_o}{z_o^2 + 1}}$  as the radial damping term. The behavior of the oscillating cosine term is easier to understand when we plot the set of points in  $r$  and  $\vartheta$  where it is maximum (Figure 23). We see that due to this term, the spiral pattern appears. These two terms, along with the term that comes from the Laguerre polynomial, give the beam profile of Figure 21(a).

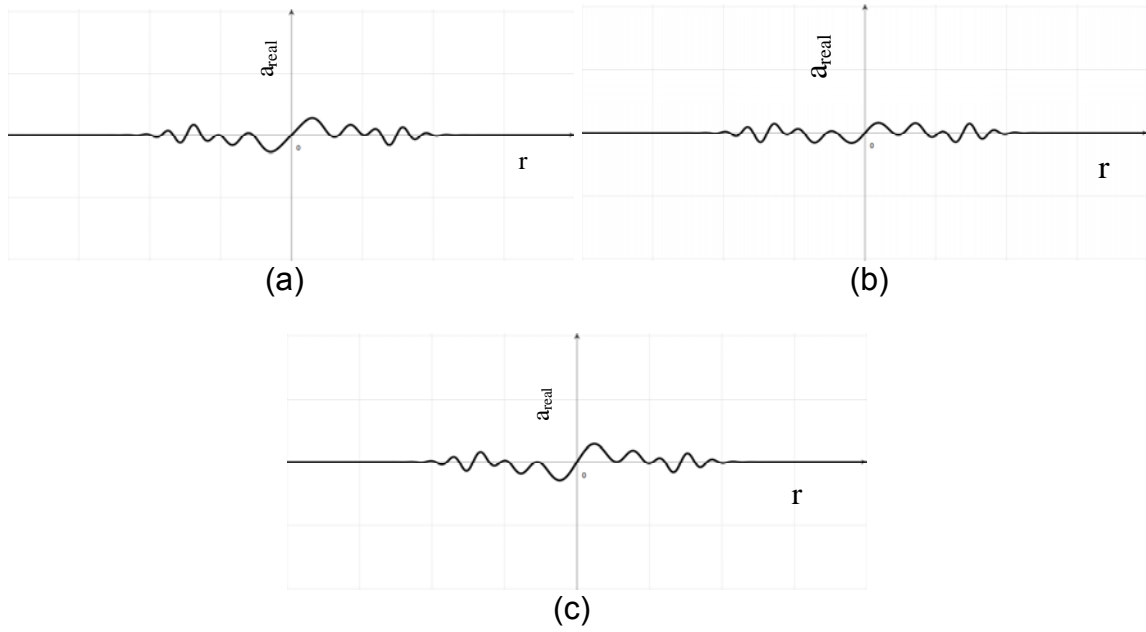


Figure 22. Radial distribution of a  $LG_2^1$  beam along (a)  $\vartheta = 0$ , (b)  $\vartheta = \pi/2$  and (c)  $\vartheta = \pi/4$ .

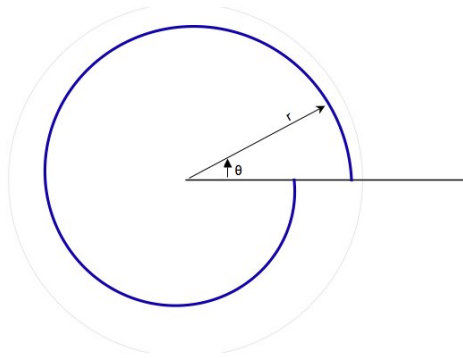


Figure 23. Set of points in  $r$  and  $\vartheta$  where the cosine term of equation (V.33) is maximum.

THIS PAGE INTENTIONALLY LEFT BLANK

## VI. HIGH-ORDER MODES IN FREE ELECTRON LASER SIMULATIONS

In previous chapters, we have studied the fundamental Gaussian optical mode as well as the higher-order modes in both rectangular and cylindrical coordinates and their propagation through a medium without any sources. The primary tool for our research was the computer code, which enabled us to solve the parabolic wave equation numerically. To analyze the operating conditions of an FEL inside the undulator, where the optical beam coincides with the electron beam, is more complex. There we must solve both the wave equation (III.52) and the pendulum equation (III.22) at the same time. At NPS, the FEL research group has developed computer codes that solve these two equations simultaneously, and they can be used to simulate various working parameters for a free electron laser system. These are powerful tools to gain deeper understanding of FEL physics and determine the importance of every operational parameter. Perhaps more importantly, it helps us to optimize FEL performance.

### A. ELECTRON BEAM TILT

One must first understand the FEL under ideal operating conditions. But in order to cover more realistic situations, we must study the system performance under non-ideal conditions. Vibrations of a mobile system for instance, might cause the electron beam to enter the undulator off-axis or at an angle. We use the three-dimensional simulations (in  $x$ ,  $y$  and  $\tau$ ) developed in the FEL research group to investigate how sensitive the FEL is to off-axis tilting and shifting. In the simulations, we use dimensionless transverse coordinates  $\tilde{x} = x\sqrt{k/2L}$ ,  $\tilde{y} = y\sqrt{k/2L}$  and the normalized time  $\tau = ct/L$ . Three-dimensional simulations were used to analyze the tolerance of the Jefferson Lab (Jlab) FEL to a tilted electron beam. The simulations discussed below, are divided into two parts.

## 1. Gain

In the first part of the Jlab simulations, we explore the gain response to the misaligned electron beam. In other words, we focus our attention on region 1 of Figure 24, which is a graph of a typical power build up of an FEL. In this region, we have just turned on the FEL so it has not yet reached steady-state. The gain is proportional to the slope of the power, in this case.

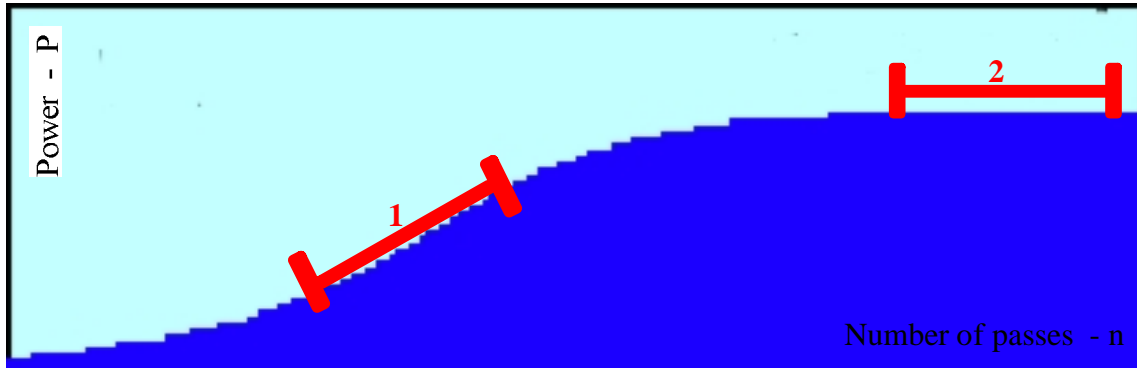


Figure 24. Simulation output, showing the power  $P$  versus number of passes  $n$  in an FEL. In the first region, power is still building up while in region 2, FEL has reached its steady-state.

We use the basic input parameters shown in Table 3, where we simulate weak fields ( $a_o = \pi$ ) and small number of passes  $n$  so as to be sure that we explore the power evolution in region 1. Also, the electron beam focus position is  $\tau_\beta = 0.5$ , so the electron beam is focused at the center of the undulator. We thus run our simulations by varying the tilt angle about the center of the undulator.

We also normalize the tilt angle of the electron beam to the undulator length and the optical wavelength

$$\tilde{g}_{yo} = \frac{g_{yo}}{\sqrt{\lambda/\pi L}} \approx \frac{g_{yo}}{(426 \text{ mrad})} \quad \text{for the Jlab parameters.} \quad (\text{VI.1})$$

Rayleigh Length $z_o$	0.42
Initial Optical Field Amplitude $a_o$	0.001
Current Density $j$	20.0
Number of Undulator Periods $N$	30
Number of Passes $n$	30
Electron Beam Focus Position $\tau_\beta$	0.5
Optical Waist Position $\tau_w$	0.5
Cavity Quality Factor $Q_n$	17.0

Table 3. The basic dimensionless parameters used in the Jefferson Lab FEL simulations for the Gain.

We vary the normalized tilt angle  $\tilde{\vartheta}_{y_o}$  from 0 to 4. To run the simulations, we enter the parameters of Table 3 and a range for the initial phase velocity  $\nu_o$ . The optimum value of  $\nu_o$  is determined in this way and we then look at the output of the run with this specific phase velocity  $\nu_o$ . In Figure 25, we show a sample output for  $\tilde{\vartheta}_{y_o} = 2.0$ , where the optimum initial phase velocity was found to be  $\nu_o = 5.5$ .

The dimensionless input parameters are shown in the upper-right box of Figure 25. On the upper-left graph, we plot the evolution of a slice of the optical beam at the outcoupling mirror, over the number of passes  $n$ , along with the color scale for the intensity plots of the optical field amplitude. Next to it, there is a 3-D representation of the beam shape after the last pass, again at the outcoupling mirror. Below the 3-D graph, we plot the cross-section of the optical beam  $|a(0, y, \tau)|$  (yellow) and the electron beam (red) inside the undulator, at the

last pass. Further down, there is a graph of the evolution of the phase velocity distribution over the number of passes  $f(v,n)$ , and next to it there is a phase-space plot of the electrons at the end of the undulator. Below the parameter table, there are two plots which show the development of the optical power  $P(n)$  and the gain  $G(n)$ . In the next row, there are graphs at both the outcoupling and the left mirror after the last pass, showing the optical beam transverse profile (yellow) compared to the theoretical Gaussian (purple), and the optical phase. Also shown in the same graphs is the intensity of the light (using the color scale at the top) and the extent of the mirrors (black). At the bottom, there is a list of the calculated results and in the lower right we plot the coefficients of the modes  $|c(m,n)|$  that comprise the beam at the outcoupling mirror after the last pass. The modal analysis is performed in terms of the Hermite-Gaussian modes. In the simulation results of Figure 25 we see that the output beam comprises basically from the fundamental mode ( $m = n = 0$ ) but simulation predicts that there will be few higher-order modes in the beam structure as well. This is shown with the plotted squares (lighter blue color). Using this tool, we can look at the mode composition of any arbitrary wavefront that our simulations predict as the laser output.

Figure 26 is a summary of the results showing gain  $G$  versus electron beam tilt angle  $\tilde{\theta}_{yo}$ . We note that the FEL can operate pretty well with an imperfect electron beam injection into the undulator, since the gain falls to half of its peak value at dimensionless tilt angle of about  $\tilde{\theta}_{yo} \approx 3.5$ , corresponding to an actual tilt of about  $1.5 \text{ mrad}$ .

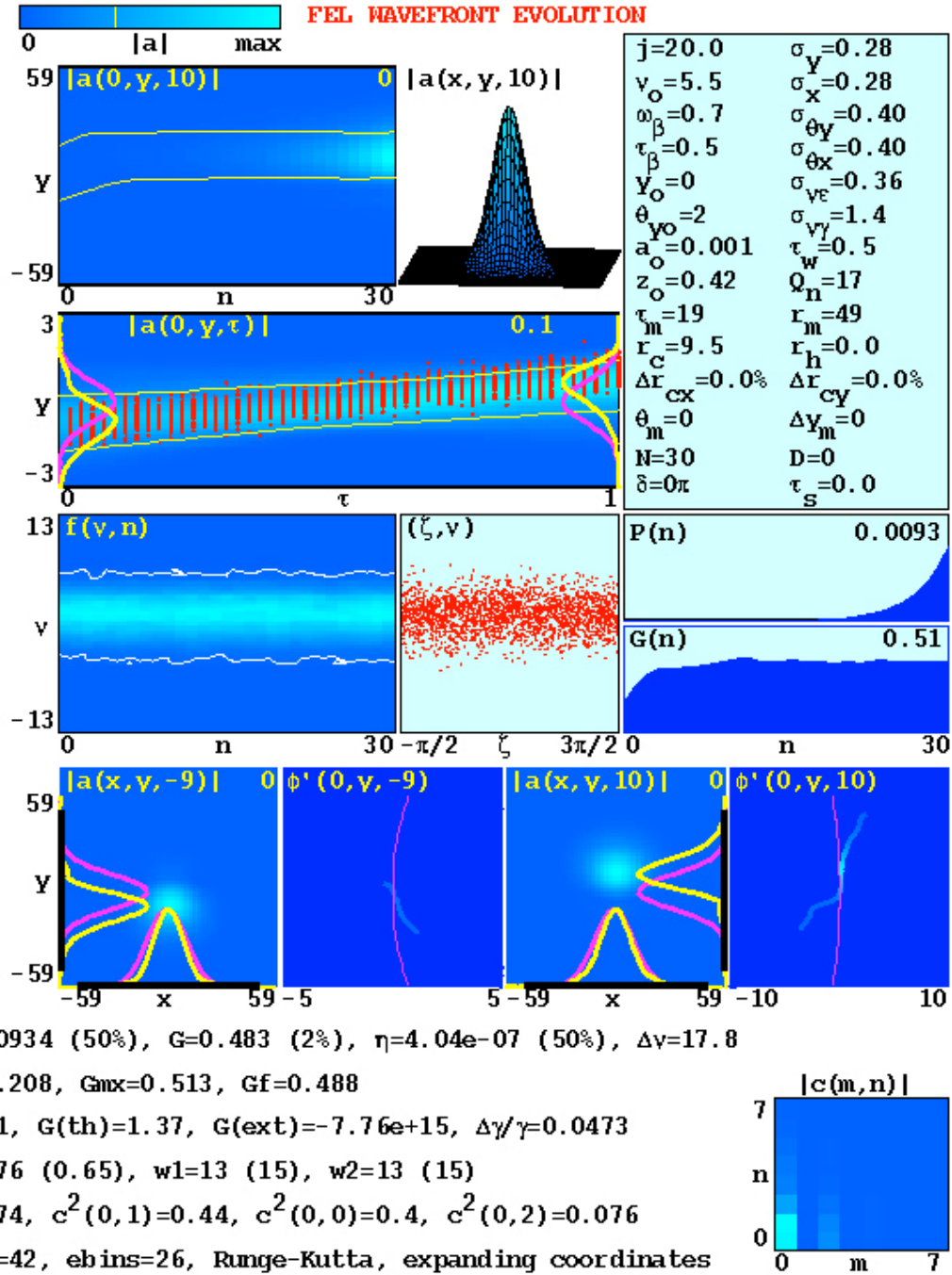


Figure 25. Output of a 3-D Simulation for Jefferson Lab FEL.

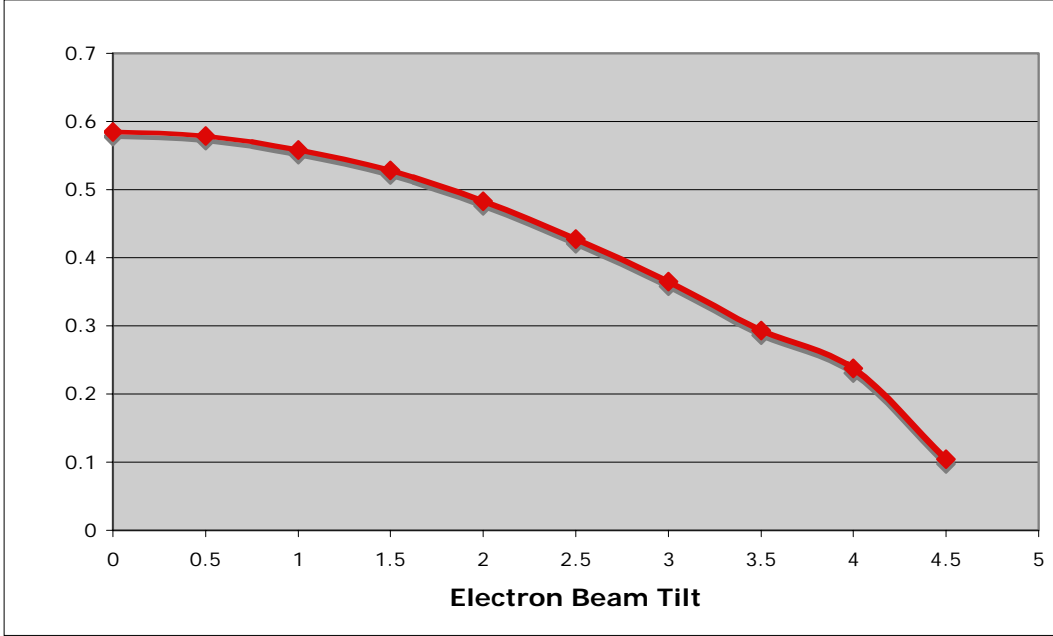


Figure 26. Summary of the simulation results for the gain versus increasing electron beam tilt angle  $\tilde{\mathcal{G}}_{yo}$ .

## 2. Extraction

Having explored how the FEL responds to a tilted electron beam during the early stages of its operation, we can now explore the effects during its steady state phase, region 2 of the graph in Figure 24. So we choose strong initial optical fields  $a_o$  and large number of passes  $n$ , as shown in the Table 4.

As a measure of the performance of the FEL in this case, we estimate the extraction  $\eta$ , defined as the fractional energy transferred from the electron beam to the optical field during one pass through the undulator

$$\eta = \frac{\text{extracted optical power}}{\text{initial electron beam power}}. \quad (\text{VI.2})$$

Rayleigh Length $z_o$	0.42
Initial Optical Field Amplitude $a_o$	10
Current Density $j$	20.0
Number of Undulator Periods $N$	30
Number of Passes $n$	500
Electron Beam Focus Position $\tau_\beta$	0.5
Optical Waist Position $\tau_w$	0.5
Cavity Quality Factor $Q_n$	17.0

Table 4. The basic dimensionless parameters used in the Jefferson Lab FEL simulations for the extraction.

Running the simulations as before, we first determine the value of the phase velocity  $v_o$  for peak extraction  $\eta$ , and then we look at the output of this particular run. One sample output for  $\tilde{g}_{y_o} = 3.0$  is shown in Figure 27, where we can verify from the power evolution graph  $P(n)$ , that the FEL is in its steady-state operation region.

nx=200, nt=50, np=30000, Wp=8, seed=7

Tue Feb 20 14:23:38 2007

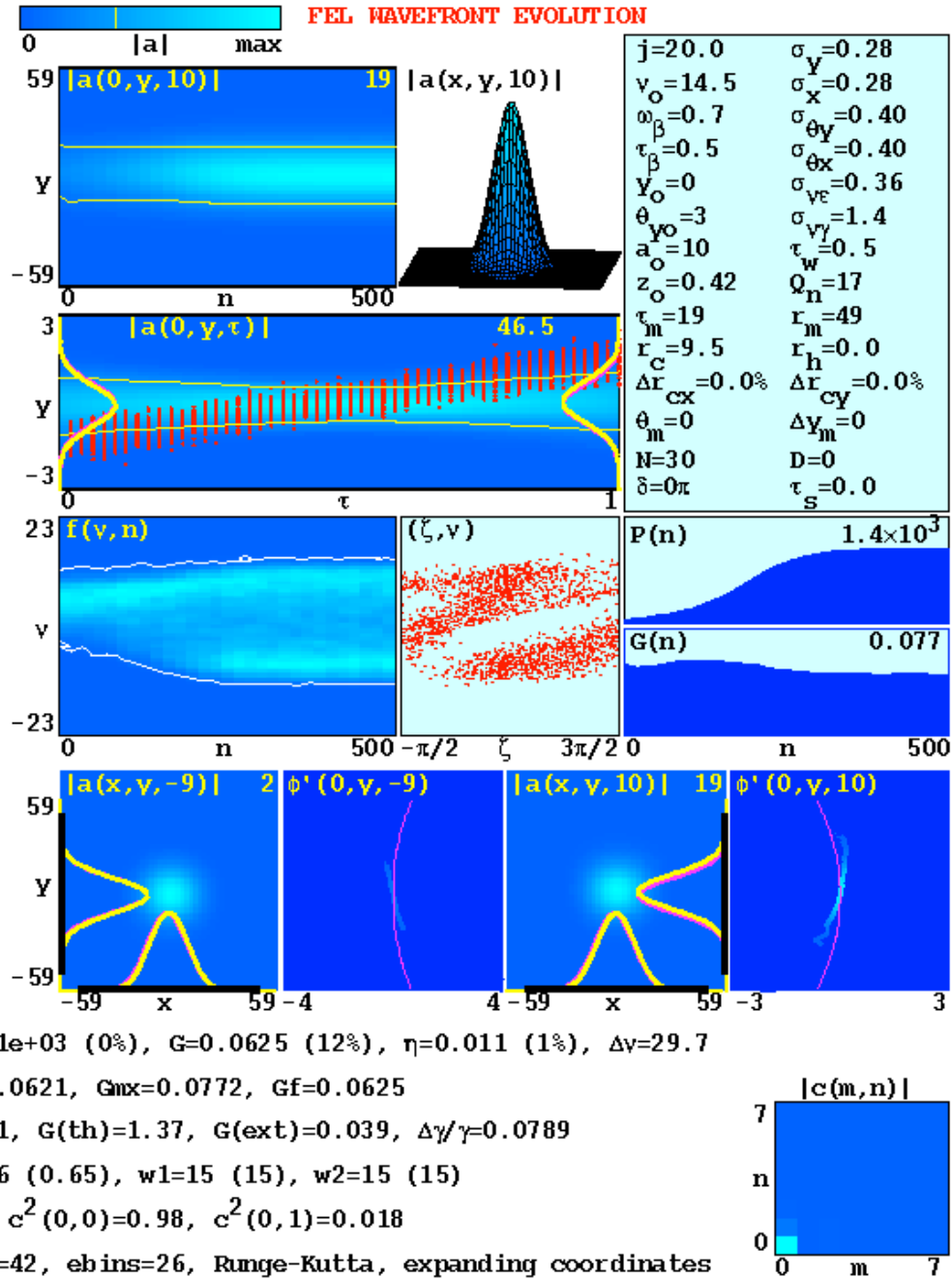


Figure 27. Output of a 3-D Simulation for Jefferson Lab FEL, exploring extraction.

Summarizing the results for many tilt angles  $\tilde{\vartheta}_{yo}$ , we note with some surprise that the FEL exhibits good tolerance; the extraction actually increases with increasing angles  $\tilde{\vartheta}_{yo}$ , up to a point, as shown in Figure 28. This may be due to “overbunching” of the electrons when there is no tilt, reducing the extraction in that case. The simulation predicts extraction greater than 1% for normalized beam tilt  $\tilde{\vartheta}_{yo} < 3$ , corresponding to an actual tilt about  $1.3\text{ mrad}$ .

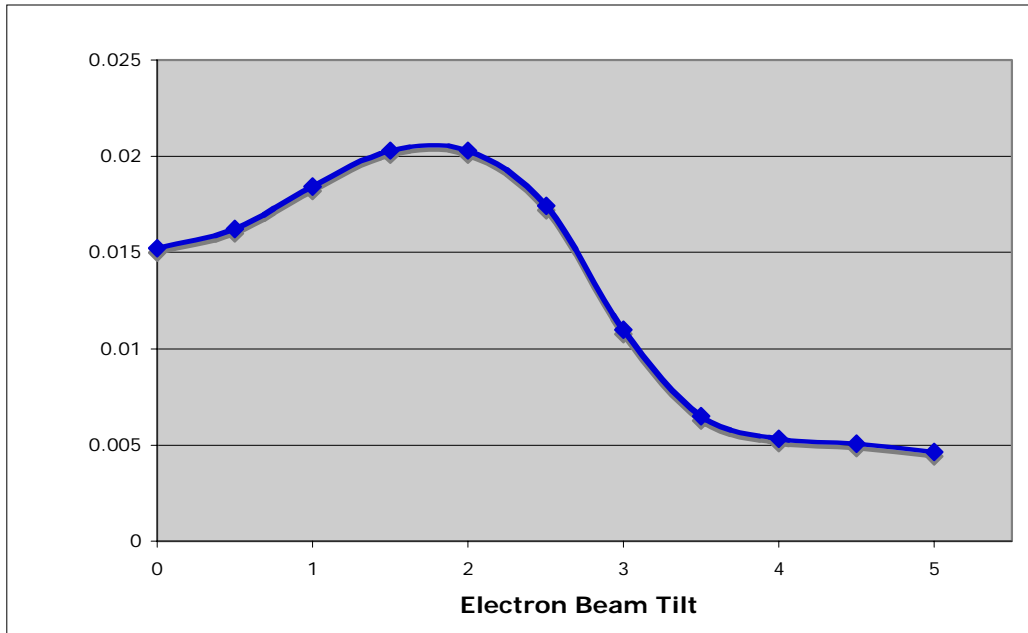


Figure 28. Summary of the simulation results for the extraction  $\eta$  versus increasing electron beam tilt angle  $\tilde{\vartheta}_{yo}$ .

THIS PAGE INTENTIONALLY LEFT BLANK

## VII. CONCLUSION

In this thesis, after reviewing the basic FEL and optical theory, we found solutions to the parabolic wave equation that suggest the existence of higher-order optical modes, working with either rectangular or cylindrical coordinates. Motivated by the symmetry of the FEL system, we focused our attention on the solutions derived using cylindrical coordinates, which employed Laguerre polynomials. Analyzing the Laguerre-Gaussian modes, we found interesting results for the beam shape and for the beam evolution as well. The modal analysis showed us that we have to consider the physical attributes of light, in order to explain the unexpected behavior of the laser beam after its propagation. Particularly, we noticed spiral patterns in the beam, attributed to the orbital angular momentum of light. Finally, we demonstrated the appearance of higher-order modes in an FEL output, while investigating the tolerance of the Jefferson Lab FEL to electron beam tilt.

Currently, the NPS FEL research group is analyzing the output wavefronts of computer simulations in terms of Hermite-Gaussian modes. We suggest that a future thesis work would develop a function that analyzes an arbitrary wavefront from an FEL simulation in terms of the Laguerre-Gaussian modes. The use of this tool could make the optical beam analysis of any simulated FEL output more complete, helping us understand better the effects of the investigating operating parameters.

THIS PAGE INTENTIONALLY LEFT BLANK

## LIST OF REFERENCES

- [1] Thomas Jefferson Lab National Facility, *Free electron laser system diagram*, <http://www.jlab.org/FEL/feldescrip.html>, 3 March 2007.
- [2] The BESSY SASE FEL, <http://www.bessy.de>, 2 March 2007.
- [3] Joachim Stohr, Stanford Synchrotron Radiation Laboratory, Linac Coherent Light Source, *Toward an X-Ray Free Electron Laser*, 2 February 2007.
- [4] Thomas Jefferson Lab National Accelerator Facility, *Annual Review*, 17 January 2007.
- [5] Duke University, FEL Laboratory, <http://www.fel.duke.edu>, 20 March 2007.
- [6] W.B. Colson, C. Pellegrini and A. Renieri, *Free Electron Laser Handbook*, Volume 6, Chapter 5, North-Holland Physics, 1990.
- [7] H. Kogelnik and T. Li, *Laser Beams and Resonators*, Applied Optics, Vol. 5, No. 10, 1966.
- [8] R.Vigil, *Hermite-Gaussian Modes and Mirror Distortions in the Free Electron Laser*, Master's Thesis, Naval Postgraduate School, 2006.
- [9] Wolfram Mathworld, *Laguerre Differential Equation*, <http://mathworld.wolfram.com/LaguerreDifferentialEquation.html>, 30 April 2007.
- [10] P. Crawford, M. Pysher, H. Sztul and P.J. Haglin, *Light Beams in High-Order Modes*, <http://departments.colgate.edu/physics/research/optics/oamgp/gp.htm>, 17 January 2007.
- [11] L. Allen, M. W. Beijersbergen, R. J. C. Spreeuw and J. P. Woerdman, Phys. Rev. A, 45, 8185, 1992.
- [12] B. Williams, *Higher-Order Modes in Free Electron Lasers*, Master's Thesis, Naval Postgraduate School, 2005.
- [13] SpringerLink, *Laguerre Polynomials*, <http://eom.springer.de//I057310.htm>, 20 November 2006.
- [14] D. J. Griffiths, *Introduction to Electrodynamics*, Prentice Hall, 1999.

- [15] F. L. Pedrotti, L. S. Pedrotti and L. M. Pedrotti, *Introduction to Optics*, Third Edition, Prentice Hall, 2006.

## INITIAL DISTRIBUTION LIST

1. Defense Technical Information Center  
Ft. Belvoir, Virginia
2. Dudley Knox Library  
Naval Postgraduate School  
Monterey, California
3. Professor William Colson  
Naval Postgraduate School  
Monterey, California
4. Professor Robert Armstead  
Naval Postgraduate School  
Monterey, California
5. Professor Joseph Blau  
Naval Postgraduate School  
Monterey, California
6. Professor Peter Crooker  
Naval Postgraduate School  
Monterey, California
7. Chairman, Physics Department  
Naval Postgraduate School  
Monterey, California
8. Air Attache  
Embassy of Greece  
Washington, DC